Bulletin of Physics Projects
Journal homepage: http://www.bbcphysics.in/index.php/journal

FEATURED ARTICLE

The North Indian Ocean

Anant Parekh[#] and Mahen Konwar

Indian Institute of Tropical Meteorology, Pune 411 008, Maharashtra, India

[#]E-mail address: anant@tropmet.res.in

The north Indian Ocean, among all three tropical ocean basins, is unique in several respects; the most striking difference is the seasonal reversal of the monsoon winds (blowing from the southwest during the summer monsoon and from the northeast during the winter monsoon) and its effects on the ocean currents. The summer monsoon winds are much stronger than the winter monsoon winds; hence the annual mean winds over the basin are southwesterly. This temporal asymmetry extends to rainfall, with most of (80%) of the rainfall over the NIO and the Indian subcontinent occurring during the summer monsoon. The Indian Ocean is the smallest, land blocked in the north, and the least sampled and understood. It can be divided into three major areas: the equatorial belt stretching between 10° N and 10° S, with the Somali basin on its western end, the Bay of Bengal (BoB) in the east and the Arabian Sea (AS) in the west.

Features of Arabian Sea and Bay of Bengal

There exist geographical similarities between the AS and BoB basins: both are located in the same latitude band and are semi-enclosed basins that open in to the equatorial Indian Ocean in the south. There are also meteorological similarities: both are forced by the changing monsoon winds and receive similar amounts of solar radiation at the top of the troposphere. They also show dramatic response to the local and remote atmospheric forcing due to wind stress, heat and fresh water fluxes associated with the monsoon and meteorological disturbances [Shenoi et al., 2002]

In spite of this, there are striking dissimilarities between the two basins. First, the winds over the two basins are different, this difference being most striking during the summer monsoon. This is a consequence of the AS being bounded on its west by highlands of East Africa. These highlands serve as the western boundary for the low-level atmospheric flow, leading to the formation of an atmospheric "western boundary current" just like in the oceans. The resulting low level jet called the Findlater Jet [Findlater, 1969], makes the winds over the AS more than twice as strong as those over the BoB, which does not experience a similar western boundary effect. Second is precipitation exceeds evaporation in the BoB; while evaporation exceeds precipitation in the AS. Annual rainfall over the BoB varies from 1m off southeast India to more than 3 m in the Andaman Sea and coastal region north of it; annual rainfall over AS is barely 1 m. The BoB receives an annual runoff of 1.5 X 10^{12} m^3 from rivers flowing into it, the runoff from the Ganga and Brahamputra into the northern bay being the fourth largest in the world [Martin et al., 1981; Shetye, 1993, Varkey et al., 1996]; runoff from rivers into the AS is meager. Therefore the surface layer in the BoB is much fresher than that in the AS; the average salinity of the top 50m in the AS exceeds that in the Bay by nearly 3 psu. The large inflow of fresh water from precipitation and runoff results in strong near surface stratification in the Bay. Figure 1.1, shows rainfall and river runoff information over the AS and BoB.

The spatial distribution of the upper ocean salinity between the AS and the BoB is also strikingly different. The salinity in the AS gradually increases towards the north. It increases from 35.5 psu at the equator to 36.5 psu north of 15 ° N. On the other hand, high-salinity water of the BoB is located in the equatorial region with a trend decreasing northward. It decreases from 34.6 psu at the equator to 33.2 psu in the northern bay, which is about 3 psu fresher than that in the northern AS (figure 1.2). In addition to the differences in horizontal distribution of salinity between the AS and BoB, the vertical distribution

of salinity also differs considerably between the two basins [Levitus, 1994]. The rapid increase in salinity with depth near the surface, commonly observed in the BoB is not seen in the AS, where salinity in the top 50m is greater than that below [Prasad, 2004]. The profile in the Bay also shows striking temperature inversions, these being most common during winter [Shetye et al., 1996, Shenoi et al., 2002, and Thadathil et al. 2002].

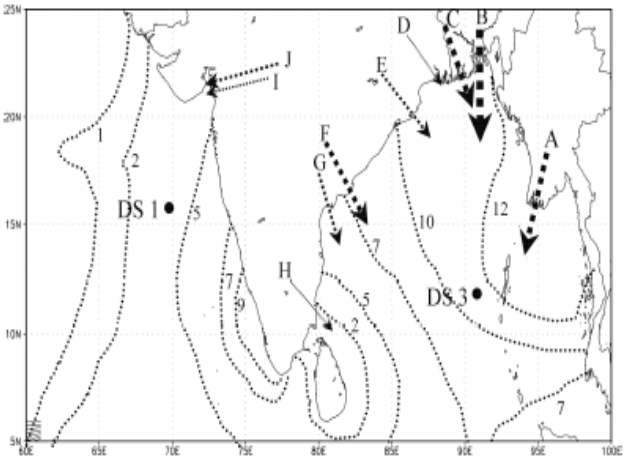

Figure 1: North Indian Ocean basin with the moored buoy (DS1 and DS3) locations. Contours show the daily averaged rainfall (mm/day) and the arrows indicate run-offs of the major rivers in the region during the summer monsoon period, viz. A, Irrawaddy; B, Brahmaputra; C, Ganga; D, Damodar; E, Mahanadi; F, Godawari; G, Krishna; H, Cauvery; I, Tapi and J, Narmada. Arrow thickness roughly indicates runoff magnitudes for summer monsoon [Parekh et al., 2004, Varkey et al., 1996].

Prior to onset of the summer monsoon, during April-May the NIO becomes the warmest area among the world oceans [Joseph, 1990]. Soon after the onset of the monsoon in June, the winds strengthen, and SST decreases. The AS cools rapidly, but SST in the BoB remains higher than 28° C, the threshold for deep convection in the atmosphere over tropical oceans [Gadgil et al., 1984: Graham and Barnett, 1987; Sud et al., 1999]. This difference in SST is reflected in the convective activity in the atmosphere, with the convection over the BoB being perhaps the largest in the tropics during summer. The convective activity associated with the summer monsoon, which has been recognized as an important source of energy for the tropical circulation [Krishnamurti, 1971] is maximum in northern BoB. The numbers of low-pressure systems that form there by far exceed those in the rest of the NIO [Mooley and Shukla, 1989]. These low-pressure systems move westward over India [Sikka, 1977; Goswami, 1987] and bring rainfall to central and northern India. It is in contact with the equator along its eastern boundary, hence it can support rapidly propagating planetary waves and in the presence of the seasonal wind it can generate low frequency waves.

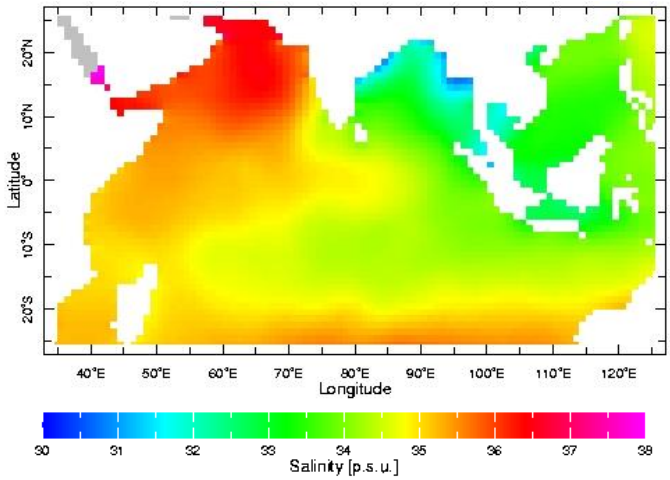

Figure 2: Surface Salinity over the north Indian Ocean in psu (Levitus Climatology).

Annual cycle of SST over the Arabian Sea and Bay of Bengal

During January-February, SST in the NIO is less than 28° C, except for a small region off southwest India [Shenoi et al., 1999]. SST rises gradually as the Sun moves pole-ward over the Northern hemisphere, with the BoB warming faster than AS. SST exceeds 30°C over most of the NIO by May; for the week centered on 15 May, surface water having temperatures greater than 30°C occupies 40 % of the total area of the AS and 63% of the total area of the BoB. With the onset of summer monsoon in June, SST starts falling in both basins and continues to fall until the end of August. For the week centered on 14th August, surface water having temperatures greater than 28°C occupies about 17% of the AS and 100% of the BoB. Once the summer monsoon starts to collapse in September, both basins start warming again [Shenoi et al., 2002]. The cold, dry continental winds that blow from the northeast cool the basins again in November, this phase lasting till February. Three major conclusions can be drawn from the evolution of SST. First, though both the AS and the BoB show a bimodal SST distribution in time [Vinayachandran and Shetye, 1991], the latter remains warmer throughout the year. Second, the northern BoB (NBoB) is warmer than the rest of the BoB during the summer monsoon. Third, SST in the AS exhibits a distinct spatial gradient, with SST in the west being less than in the east.

Monsoon and Indian Ocean

Monsoon derives from the Arabic word 'mausam', meaning season. Many regions of the tropics and

subtropics experience a rainy summer season and a dry winter season. The main driver of this marked seasonality in rainfall is the change in the distribution of surface heating between winter and summer, primarily associated with seasonal variations in the position of the sun. Because of this close relationship with the solar seasonal cycle, the start of the rainy season often begins with remarkable regularity each year. It is also considered a manifestation of the seasonal variation of the Tropical Convergence Zone (TCZ), which migrates onto the Indian subcontinent in the northern hemispheric summer. A TCZ is characterized by convergence of moist air in the lower troposphere and strong ascent up to the upper troposphere leading to deep convective clouds [Gadgil, 2000]. A TCZ can extend over thousands of kilometers in the east-west direction but its latitudinal extent is relatively small, seldom exceeding ± 10°.The large-scale rainfall during the summer monsoon (June–September) over the Indian region is associated with the occurrence of a TCZ over the heated subcontinent. A TCZ occurs over the equatorial Indian Ocean in the pre-monsoon months of April and May. During the onset phase, the TCZ propagates across the peninsula and gets established near its seasonal mean location over the Indo- Gangetic plains. At intervals of 2–6 weeks, this oceanic TCZ propagates onto the subcontinent in a manner similar to that of the onset phase. These northward propagations of TCZ across the BoB and eastern AS play an important role in maintaining the continental TCZ. Variability of the continental TCZ and hence the monsoon is therefore, linked to the variability of convection over these warm oceans. Thus summer monsoon is an important component of the tropical coupled atmosphere/ocean system and needs to be accurately represented in models in order to increase predictability on the global scale.

References

Shenoi, S. S. C., Shankar, D and Shetye, S. R., 2002. Differences in heat budgets of the near-surface Arabian Sea and the Bay of Bengal: Implications for the summer monsoon, 2002, Jour. Geophys. Res., 107(6), 10.1029.

Findlater, J., 1969. A major low-level air current near the Indian Ocean during the northern summer, Q. J. R. Meteorol. Soc., 95, 362-380.

Martin, J. M., J. D. Burton, and D. Eisma, River Inputs to Ocean Systems,United Nations Press, New York, 1981.

Shetye,S. R. 1993, The movement and implications of the Ganges-Brahmaputra runoff on entering the Bay of Bengal, Curr. Sci., 32– 38, 1993.

Varkey, M. J., Murty, V. S. N. and Suryanarayana, A., *Oceanogr. Mar. Biol., Annu. Rev.*, 1996, **34**, 1–70.

Levitus, S., R. Burgett, and T. P. Boyer, World Ocean Atlas 1994, vol. 3, Salinity, NOAA Atlas NESDIS, vol. 3, 111 pp., Natl. Oceanic and Atmos. Admin., Silver Spring, Md., 1994.

Prasad, T. G, 2004. A comparison of mixed-layer dynamics between the Arabian Sea and Bay of Bengal: One-dimensional model results, J. Geophys. Res., 109, C03035 (1-15).

Parekh A., A. Sarkar, S. Shah and M S Narayanan, Low period variability in TMI measured SST over the Bay of Bengal during summer monsoon, Current Science,2004, 87, 791-796.

Shetye, S. R., A. D. Gouveia, D. Shankar, G. S. Michael and G. Nampoothiri, 1996, Hydrography and circulation of the western Bay of Bengal during the northeast monsoon, J. Geophys. Res., 101, 14,011-14,025.

Joseph, P. V., Warm pool over the Indian Ocean and monsoon onset, Tropical Ocean and Atmosphere Newsletter, 53, 1 –5, 1990.

Gadgil, S., P. V. Joseph, and N. V. Joshi, Ocean-atmosphere coupling over monsoon regions, Nature, 312, 141– 143, 1984.

Gadgil S. 2000. Monsoon-ocean coupling.Curr. Sci. 78:309–23.

Graham, N. E., and T. P. Barnett, Observations of sea-surface temperature and convection over tropical oceans, Science, 238, 657– 659, 1987.

Sud, Y. C., G. K. Walker, and K.-M. Lau, Mechanisms regulating sea surface temperatures and deep convection in the tropics, Geophys. Res. Lett., 26, 1019– 1022, 1999.

Krishnamurti, T. N., Tropical east-west circulations during northern summer, J. Atmos. Sci., 28, 1342– 1347, 1971.

Mooley, D. A., and J. Shukla, Main features of the westward-moving low pressure systems which form over the Indian region during the summer monsoon season and their relation to the monsoon rainfall, Mausam, 40, 137– 152, 1989.

Sikka, D. R., Some aspects of the life history, structure of movement of monsoon depressions, in Monsoon Dynamics, PAGEOPH, vol. 115, edited by T. N. Krishnamurti, pp. 1501– 1529, Birkha¨user Boston, Cambridge, Mass., 1977.

Goswami, B. N., A mechanism for the west-northwest movement of monsoon depressions, Nature, 326, 376–377, 1987.

Shenoi, S. S. C., D. Shankar, and S. R. Shetye, On the sea surface temperature high in the Lakshadweep Sea before the onset of the southwest monsoon, J. Geophys. Res., 104, 15,703–15,712, 1999.

Thadathil, P., V. V. Gopalakrishna, P. M. Muraleedharan, G. V. Reddy, N. Araligidad, and S. Shenoy (2002), Surface layer temperature inversion in the Bay of Bengal, Deep-Sea Res., 49, 1801–1818.

Vinayachandran, P. N., Shetye, S. R., The warm pool in the Indian Ocean, Proceeding of the Indian Academy of Science (Earth and Planet Science), 100(2), 165-175,1991.

Bulletin of Physics Projects 2, 2017, 4-7 ISSN No: 2455-9407

Bulletin of Physics Projects

Journal homepage: http://www.bbcphysics.in/index.php/journal

An Analytical Study of the Dependence of Ripple Factor on Load Resistance in L-Section Filter

Bikram Rajkhowa and Diganta Kumar Sarma[#]

Department of Physics, B. Borooah College, Ulubari, Guwahati-781007, Assam, India

[#]E-mail address: sarma.diganta@gmail.com

Abstract

This work deals with the study of dependence of ripple factor on load resistance in L-section filter. The theoretical expression of ripple factor in case of L-section filter has been derived for ideal arrangement where the resistances of the inductor, diode and the transformer secondary is considered to be zero. But in practice these elements have some high value (~500 ohm). Beside this the value of the inductive reactance should be high enough compared to the impedance of the parallel combination of the capacitors and the load. An attempt has been made here to find a suitable value of L and load resistance for which the theoretical relation becomes valid and the ripple factor becomes independent of the load resistance value.

1. Introduction

Filter circuits are used to remove the ac components of a rectifier output. They are used in many devices which run on dc current, where a steady voltage is required. There are various types of filter circuits such as capacitor filters, L-section filter, T-section filter, etc. these filters are basically a combination of capacitors and inductors. A capacitor passes ac readily but does not pass dc, whereas an inductor opposes ac but allows dc to pass through it. Thus a suitable network of inductors and capacitors can effectively remove the ac component allowing the dc component to reach the load.

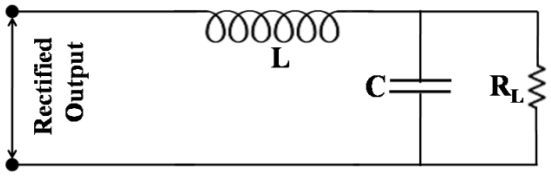

Figure 1: Circuit diagram of an L-section Filter

In the figure L and C are inductor and capacitor respectively. R_L is the load resistance. The ripple factor of an L-section filter is given by $r=1/6\sqrt{2}\omega^2LC$, where, ω is the angular frequency, L is the inductance, C is the capacitance. In the formula given above we can see that the ripple factor is independent of load resistance. Our objective is to verify this fact experimentally. The main objective of the present study is to see the variation of ripple factor of L-section filters with load resistance.

2. Methodology and data analysis:

The schematic diagram shows the methodology adopted for the present study. An AC source and connect it to a full wave rectifier. The output of the rectifier is fed as the input of the L- section filter. The voltage across the load resistance is measured using a CRO. The ratio of ac voltage to dc voltage gives the ripple factor, $r = V_{ac}/V_{dc.}$. The above processes are repeated for different values of load resistances. After that a graph is plotted between the load resistance and corresponding ripple factor.

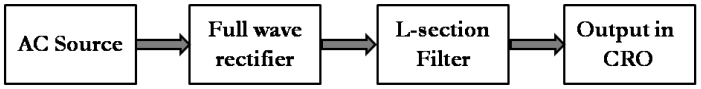

Figure 2: Schematic diagram of the methodology

Table I shows the ac and dc voltages across the load resistance and the corresponding theoretical ripple factors values. The values considered for inductance and capacitance are: Inductance (L) = 6 H, Capacitance (C) = 0.1μF, $\omega = 2\pi \times 50 = 314.16$ rad /sec.

Table I: Ripple factors of the L-section filter for different values of load resistances

Sl. No.	Load resistance R_L (Ω)	V_{PP} (Volts)	$V_{ac}=\frac{V_{PP}}{2\sqrt{3}}$ (Volts)	V_{dc} (Volts)	$r=\frac{V_{ac}}{V_{dc}}$	r (Theoretical)
1	500	1.6	0.461	3.5	0.132	
2	1000	2.8	0.808	5.4	0.149	
3	3000	7.2	2.078	8.6	0.242	
4	5000	11	3.175	10	0.317	
5	7000	13	3.753	10	0.375	
6	10,000	14	4.04	10	0.404	
7	12,000	15	4.33	11	0.43	
8	14,000	15	4.33	11	0.39	1.99
9	16,000	15	4.33	11	0.39	
10	18,000	15	4.33	11.5	0.39	
11	20,000	16	4.62	12	0.38	
12	22,000	16	4.62	12	0.38	
13	24,000	16	4.62	12	0.38	
14	26,000	16	4.62	12	0.38	
15	28,000	16	4.62	12	0.38	
16	30,000	15.5	4.47	11.8	0.38	

3. Results and Discussions

A graph is drawn taking load resistance on the X-axis and ripple factor on the Y-axis as shown in Fig. 3. It can be seen from the graph that ripple factor is almost constant after about 14,000Ω. But below 14,000 Ω, the ripple factor has quite an unexpected variation. The possible reasons for this behavior can be as follows: Some assumptions are made while deriving the formula for the ripple factor. Thus the theoretical formula for the ripple factor, $r=1/6\sqrt{2}\omega^2 LC$, is true only for an ideal arrangement where the resistance of the inductor, the diodes and the transformer secondary is zero. But in reality these elements have quite high resistance (at least 500 Ω for a standard arrangement). Also for the formula to be valid, the value of the inductor reactance should be quite high compared to the impedance of the parallel arrangement of the capacitor and the load resistance. Thus the value of the inductor should be in Henrys and not in milli-Henry.

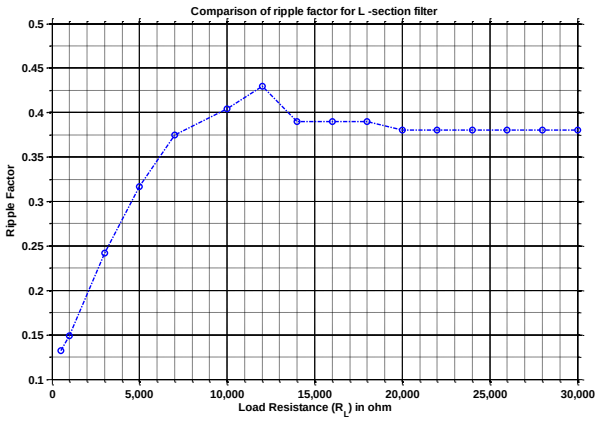

Figure 3: Variation of ripple factor with load resistance.

3.1. Derivation:

Let us consider the derivation of the formula for ripple factor of an L-section filter with full-wave rectifier.

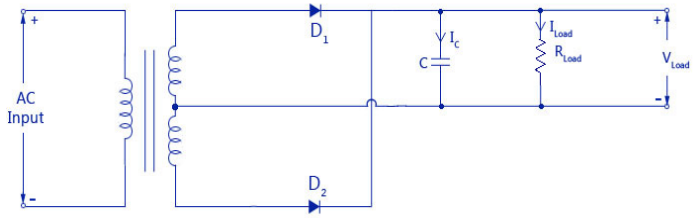

Figure 4: Circuit diagram of a full wave rectifier with L-section filter

The voltage after rectification (between points A and B) can be given by $V=2V_m/t-4V_m\cos 2\omega t/3t$, where V_m is the voltage amplified of the transformer output. This expression is obtained after Fourier series representation of the output voltage of the rectifier. The higher harmonics are neglected because they have very small amplitudes and contribute very little to the ripple. The first term $2V_m/t$ gives the dc output voltage provided the resistance of the inductor, the diodes and the transformer secondary is neglected. Thus $[V_{dc}]_{ideal}=V_m/t$. But if the resistances are taken into account then $V_{dc}=v_m/t- I_{dc}R$, where R is the total resistance of the inductor, the diodes, and the transformer secondary.

Now if the impedance of the inductor is large enough, the impedance of the load resistor and capacitor in parallel can be neglected. Taking this assumption, we have the impedance across AB is $X_L=2\omega L$, the reactance of the inductor at the 2nd harmonic frequency. But it can be shown that for low load resistances (upto about 5000Ω) the impedance of the parallel arrangement can be quite high, thus violating the assumption. So, for the assumption to be valid, we take the load resistance more than 5000 Ω (preferably more than 10,000 Ω) to get desired results.

Now the alternating voltage through the circuit is:

$V'_{rms}=\frac{\frac{4Vm}{3t}}{\sqrt{2}}=\frac{4Vm}{3\sqrt{2}t}$

$\therefore I'_{rms}= V'_{rms}/X_L=4\ V'_{rms}\ /3\sqrt{2}t \times 1/X_L$

$=\sqrt{2}t/3\ V_{dc}\ 1/X_L$ [using $V_{dc}=2V_m/t$]

The ac voltage cross the load (the ripple factor) is also the voltage across the capacitor which is

$V'_{rms}= I'_{rms} x X_c= \sqrt{2}t/3\ V_{dc}\ 1/X_L.X_{c,}$

where, $X_c=1/2\omega C$ is the reactance if the capacitor at the 2nd harmonic frequency. Thus, ripple factor is then given by:

$r =V'_{rms}/V'_{dc}=\sqrt{2}\ X_c/3X_c=\sqrt{2}/3 \times 1/2\omega C \times 1/2\omega L$

$\therefore r = 1/6\sqrt{2}\omega^2 LC$

Also the preceding derivation has been made assuming that the rectifier passes current throughout the entire circle. For this to be true the ac component of the current, $I'_{ac}=\sqrt{2}I'_{rms}$, must not exceed the direct current, $I'_{dc}=V_{dc}/R_L$. Therefore, for the diode current to exist during the entire cycle, it is necessary that

$I_{dc} \geq I'_{ac}$

$= V_{dc}/R_L \geq \sqrt{2}\ I'_{rms}= (2\ V_{dc}/3) x (1/X_L)$

[$\because I'_{rms}= (\sqrt{2}/3).V_{dc}.(1/X_L)$]

Therefore $X_L \geq 2\ R_L/3$

Or $L \geq R_L/3\omega$

For a 50 Hz input, this becomes $L \geq R_L/942$, where R_L is in ohms and l in Henrys. Thus, the minimum value of L must be $R_L/942$.

The reasons mentioned above explain why the variation of ripple factor follows the trend predicted by theory at high resistances. Also the experimental and theoretical values of ripple factor are quite close. It can be mentioned here that in our previous experiments taking lower value of inductance (50mH–200mH), the experimental ripple factors were 20 to 50 times smaller than theoretical ones. Since in this experiment we have used inductance of 6 Henry, our result was 5 times smaller than the theoretical ripple factor. Based on this observation we can safely say that if we use even higher values of inductance (> 30 H), the experimental values will be even closer to the theoretical values for the range of load resistances taken in the experiment.

3.2. Verification

In order to verify the results obtained in our experiment, we see if a **π**- section filter also gives the same variation in ripple factor as an L-section filter.

The theory of **π** – section filter predicts that its ripple factor should be $r = \sqrt{2}/(8\omega^3 C_1 C_2 L R_L)$, where C_1 and C_2 are capacitors, L is the inductor, R_L is the load resistance.

We can see that ripple factor of a **π**- section filter depends on load resistance. Thus, in order to arrive at a final conclusion we compare the ripple factors of **π**-section filter for the same range of load resistances and note the difference. Figure 5 shows the comparison of the variation of the ripple factor of L &**π**-section filter.

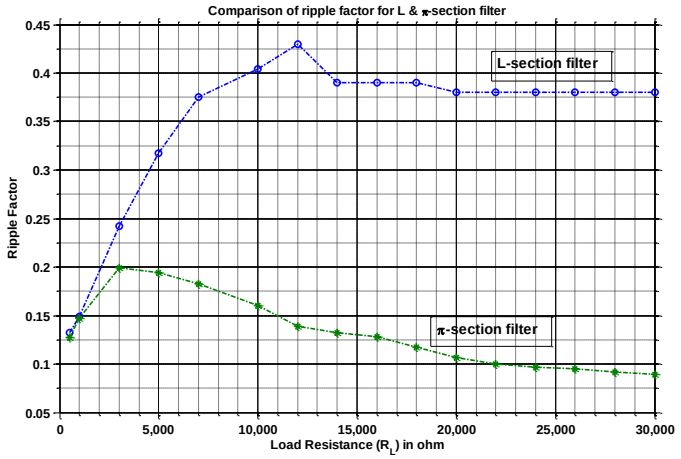

Figure 5: Comparison of the ripple factor of L & π-section filter

Table II: Ripple factors of the π - section filter for different values of load resistances

Sl. No.	Load resistance R_L (Ω)	V_{PP} (Volts)	$V_{ac}=\frac{V_{PP}}{2\sqrt{3}}$ (Volts)	V_{dc} (Volts)	$r=\frac{V_{ac}}{V_{dc}}$
1	500	1.5	0.433	3.4	0.127
2	1000	2.7	0.779	5.3	0.147
3	3000	6.2	1.789	9.0	0.199
4	5000	7.4	2.136	11	0.194
5	7000	7.6	2.194	12	0.183
6	10,000	7.5	2.165	13.5	0.160
7	12,000	6.5	1.876	13.5	0.139
8	14,000	6.4	1.847	14	0.132
9	16,000	6.2	1.789	14	0.128
10	18,000	5.9	1.703	14.5	0.117
11	20,000	5.5	1.590	14.8	0.107
12	22,000	5.2	1.500	15	0.100
13	24,000	5.1	1.470	15.1	0.097
14	26,000	5.0	1.450	15.1	0.095
15	28,000	4.9	1.415	15.3	0.092
16	30,000	4.8	1.386	15.5	0.089

It can clearly noticed that for resistances greater than 14,000 Ω the ripple factor for the L-section filter remains constant, whereas the ripple factor for **π**-section filter

decreases continuously as dictated by the theoretical formula.

The observed values of ripple factor for the **π**-section filter used in plotting this graph are given in Table II. The various parameters considered are: Inductance (L) = 6H, Capacitance C_1 = 0.1μF, C_2 = 1μF, $\omega = 2\pi x50 = 314.16$ rad/sec.

Hence, we can firmly deduce that in contrast to **π**-section filter, the ripple factor of an **L**-section filter remains constant throughout load resistance of high value.

4. Conclusions

In our experiment at hand we test the fact that ripple factor of an L-section filter remains constant for varying load resistances. In order to do this we rig a household ac source to a step down transform with center – tap. The transformer output is connected to a full wave rectifier and rectifier output is connected to an L-section filter. We measure the ac and dc voltage drop across the load resistance using CRO. After taking readings for different load resistances we find the ripple factor for each of them. A graph between load resistance and ripple factor id plotted. From the graph it is observed that the ripple factor initially varies, but after 14 k Ω it becomes constant. Thus we can infer that the theory for L-section filter holds good at high load resistances only. In order to verify this inference we assemble a full-wave **π** – section filter and observe the variation of ripple factor for the same range of load resistances used before. We can see that this time the ripple factor has a steady decline after about 14 k Ω. This finally confirms the inference drawn in the case of L-section filter. Thus we can firmly conclude that for high load resistances, the ripple factor of an L-section filter becomes constant.

5. Acknowledgement

The authors would like to thank the Principal, B. Borooah College for his support and also to the head of the Department of Physics for his valuable advice

6. References

[1] Millman and Halkias, (1972). Electronic Devices and Circuit, McGraw – Hill, Kogakusha Ltd.
[2] Mehta, V K., Principles of Electronics, S Chand Publishing
[3] Schultz M. E., (2007)Grob'sBasic electronics, Tata McGraw – Hill,
[4] https://www.digikey.com/Web%20Export/.../excelsys-measuring -ripple-noise.pdf
[5] https://e2e.ti.com/support/power_management/simple switcher/w/simple_switcher_wiki/2243.understanding measuring-and-reducing-output-voltage-ripple
[6] http://archive.ericsson.net/service/internet/picov/get ?DocNo=28701-EN/LZT146097

Bulletin of Physics Projects
Journal homepage: http://www.bbcphysics.in/index.php/journal

Estimation of Stefan's Constant from a low cost blackbody apparatus

Smriti Rabha and Kishore Dutta[#]

Department of Physics, Handique Girls' College, Guwahati-781001, Assam, India

[#]E-mail address: kdkishore77@gmail.com

Abstract

We design a low-cost blackbody apparatus comprising of an electric bulb as a black-body and thermometers to measure its maximum (steady-state) temperature. This allows us to estimate the Stefan's constant by measuring the effective surface area of the black-body, the effective watt of the bulb, and absolute steady-state temperature. The estimation of Stefan's constant from this apparatus turns out to be $\sigma = 5.907\times10^{-8}$W $m^{-2}K^{-4}$, which iscomparable with its standard value.

1. Introduction

A black body is an idealized physical body that absorbs all the incident electromagnetic radiation, regardless of frequency or angle of incidence. A black body in thermal equilibrium emits electromagnetic radiation called the black-body radiation. The black-body spectrum [Fig. 1] that follows Planck's law of radiation, is solely depends on its temperature and wavelength of the radiation and not by the body's shape or composition. The thermal radiation spontaneously emitted by many ordinary objects can be approximated as black-body radiation. A perfectly insulated enclosure that is in thermal equilibrium internally contains black-body radiation and will emit it through a hole made in its wall, provided the hole is small enough to have negligible effect upon the equilibrium.

The dependence of total radiation from a black-body on its temperature was first studied by Stefan who showed experimentally that the rate of emission of radiant energy by unit area of a perfectly black-body is directly proportional to the fourth power of its absolute temperature *T:*

$R_T = \sigma T^4$

where, $\sigma = 5.67\times10^{-8}$W $m^{-2}K^{-4}$is the Stefan's constant. Assuming black-body radiation as a perfect gas, Boltzmann applied the law of thermodynamics to radiation and deduces the Stefan's law theoretically. The law is thus generally referred to as Stefan-Boltzmann law.

Fig 1 depicts the schematic plots of the experimental black-body spectrum obtained from a black-body heated to different temperatures. The area under each curve represents the total energy emitted by the body at a particular temperature for the range of wavelength considered. With increase in temperature of the body, the area increases and it is found to be directly proportional to the fourth power of the absolute temperature, in accordance with the Stefan's law of black-body radiation.

Earlier laboratory methods for the determination of Stefan's constant were based on the electrical circuits comprising thermocouple and optical pyrometer. Here we

design a low-cost laboratory apparatus for the same purpose. Surprisingly, we see that the estimation coming from our experimental device is in well agreement with the theoretical estimates.

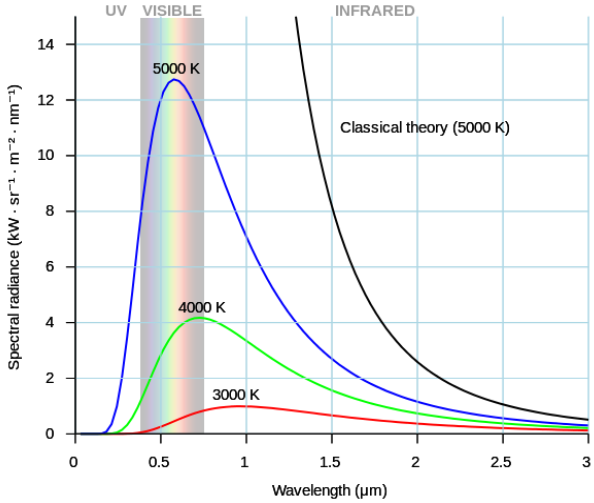

Fig. 1: A typical plot of black-body spectrum.

2. Experimental details:

The apparatus [Fig. 2] that we have designed for the purpose of investigation for the black-body radiation is a very low cost apparatus comprising an electric bulb (40 watt, 220 volt), a closed hollow chamber coated with thermocols and silver foils, three thermometers, and the domestic A.C. power line.

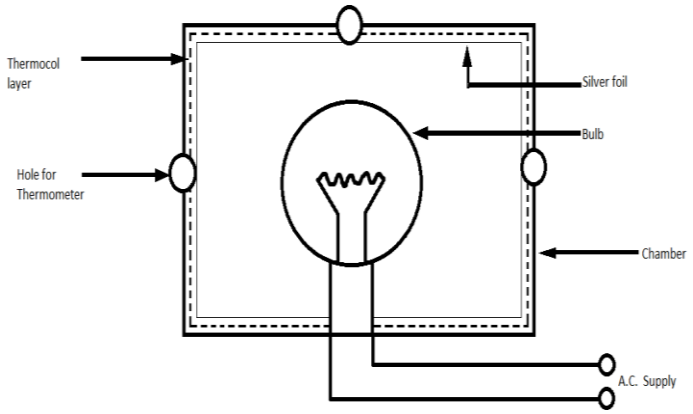

Fig 2: Schematic view of the black-body apparatus

The hollow chamber is covered with thermocollayer. The inner surface of the chamber is coated with silver foils to minimize the absorption of heat radiated by the bulb. Three holes are made in the chamber as shown in the figure.Three thermometers are then inserted through these holes to measure the maximum temperatures by touching the hot surface of the bulb. Before setting, the thermometer are to be checked whether all of them give the same room temperature inside the laboratory. Otherwise, necessary corrections are to be made.

The effective surface area of the bulb is calculated for the estimation of Stefan's' constant. The bulb is then covered with thick layers of black shoots. It thus behaves as an operative black-body for experimental purpose.

The bulb is then connected to a 220 volt a.c. supply. After few minutes the temperature of the hollow chamber increases gradually which can be recorded by the thermometers attached to the chamber. We record the temperature after every 5 minutes of interval. The temperature of the chamber gets saturated after 20 minutes and attains an almost steady state value after 30 minutes from the time of starting the experiment. We take an average value for the steady state temperature recorded by the thermometers and use it to determine the Stefan's constant.

To determine the Stefan's constant σ, we use the formula $S\sigma T^4 = W \times 10^7$(erg), where, S is the surface area of the bulb, W the effective watt,T is the absolute steady-state temperature.

3. Results and Discussions

The surface area of the bulb is estimated [Fig. 3] by calculating the respective radius for its spherical part (R_1) and (almost) conical part (R_2) together with the length (h) of the neck part. The surface area of the semi hemisphere is $\frac{1}{2}\ 4\pi R_1^2$ and the truncated conical part is $[2\pi R_1+2\pi R_2](R-h)$ where R is the radius of the semi hemisphere. The effective surface area of the bulb is thus given by

$$S = \tfrac{1}{2}\ \pi R_1^2+[2\pi R_1+2\pi R_2](R-h)$$

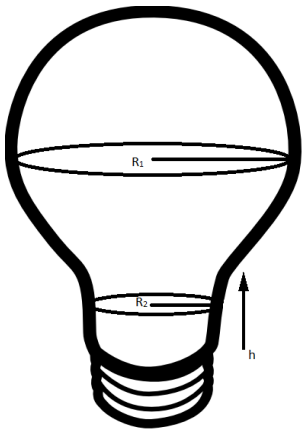

Fig 3: The parameters required for the estimation of surface area of the bulb

Measurements of R_1, R_2 and h yields $S=131.273\times10^{-4}m^2$. The effective watt W_0 of the bulb is estimated by using the formula $W_0=(v_0/v)^2$ W, where v_0 is the line voltage, v the

rating voltage, and W is the rating watt of the bulb. During our experiment, we obtain W_0=16 watt. Table I shows the records of the temperature readings taken from the three thermometers as a function of time. The steady temperature is also depicted in the Table I.

With these estimations, we calculated the Stefan-Boltzmann constant for our low-cost apparatus as:
$\sigma = w/ST^4 = 16/(379)^4 \times 131.27 \times 10^{-4}$ W $m^{-2}K^{-4}$
$= 5.907 \times 10^{-8}$ W $m^{-2}K^{-4}$
Surprisingly, our above estimated value for σ is very close to its standard value (5.67×10^{-8} W $m^{-2}K^{-4}$).

Table I: Records of the temperature readings taken from the three thermometers.

No. of Obs.	Time(minutes)	Thermometer readings			Steady temp.
		T_1 °C	T_2 °C	T_3 °C	T °C
1	5	58	71	60	
2	10	72	82	74	
3	15	79	87	86	106
4	20	88	90	94	
5	25	96	95	100	
6	30	106	105	106	
7	35	106	105	106	

4. Conclusions

In conclusion, we designed a very low-cost laboratory apparatus for the estimation of Stefan's constant. In fact, the accuracy of the experimental result depends on the accuracy in measurements of the temperature, the effective surface area of the black-body, and the effective watt of the electric bulb. This apparatus can be used for intermediate physics students to demonstrate the law of blackbody radiation. In comparison to the indirect electrical apparatus for the measurement of Stefan's constant, the present method is quite easier to perform in a laboratory. We hope our work will stimulate physics communities to proceed for developing such low-cost tools for other physical experiments.

5. Acknowledgement

The authors would like to thank the Principal, Handique Girls' College for his support and also to the head of the Department of Physics for his valuable advice.

Bulletin of Physics Projects
Journal homepage: http://www.bbcphysics.in/index.php/journal

Study of the variation of refractive index with concentration of different solutions using He-Ne Laser

Kalpajyoti Bhuyan, Rupam Sarma, Sagarika Chakraborty and Sumanta Borthakur[#]

Department of Physics, B. Borooah College, Ulubari, Guwahati-781007, Assam, India

[#]E-mail address: bormontu@gmail.com

Abstract

This work deals with the study of variation of refractive index with concentration of different solutions. A different approach is considered here in this study to measure the refractive index of the solution considered. He-Ne laser is allowed to pass through a hollow prism filled with solution. Then using spectrometry observation the refractive index is measured. It is observed that as the molar mass increases the corresponding slope of refractive index with concentration also increases for the three solutions considered.

1. Introduction

The refractive index or indices of a substance describe an important part of its interaction with electromagnetic radiation. The refractive index is a basic optical property of materials. Its accurate measurement is often needed in many branches of Physics and Chemistry and it has several applications to many industries and materials. It is measured for many reasons. It is clearly important to know the refractive index of materials used for their clarity, such as glasses and solid plastics. In complex fluids such as drinks or foods, the refractive index is a measure of dissolved or submicron material. The Brix scale relates refractive index to sugar concentration. Common industrial applications are to micro-emulsions to measure their oil/water ratio, to antifreeze to check the glycol/water ratio, and to inaccessible liquids such as the electrolyte of rechargeable cells. There are numerous methods for measuring refractive index of a liquid solution. In our project we have used the method using He-Ne laser spectrometry and hollow prism. We have utilized He-Ne laser as a light source to measure the refractive index of different standard and unknown solution.

2. Experimental details:

If a collimated beam of light AB incident on a prism of apex angle A then it gets deviated by the prism along CD as shown in the Fig. 1. i_1 and i_2 be the angle of incidence and emergence respectively. δ_m is the angle of deviation. For the minimum deviation i_1 andi_2 are equal and the refracted ray is parallel to the base of the prism. In this situation the refractive index μ of the material of the prism is related to the angle of minimum deviation δ_m by the relation

$$\mu = \frac{\sin\frac{(A+\delta_m)}{2}}{\sin\frac{A}{2}}$$

For the equilateral hollow prism A = 60^0. So measuring the value of δ_m, we can calculate the refractive index of the solution inside the hollow prism.

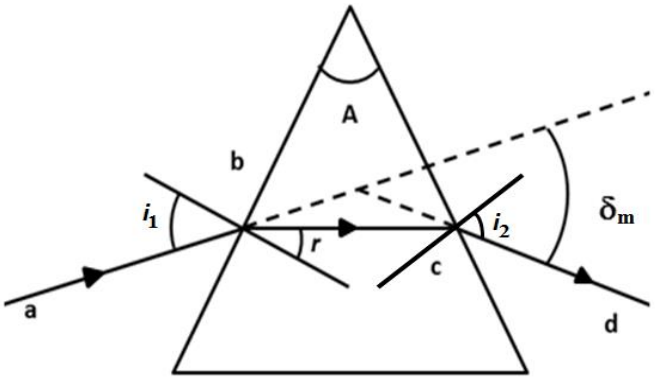

Fig. 1: Schematic diagram depicting deviation of a ray by a prism

Before using the He-Ne source, we adjusted the spectrometer using a Na light source. We balanced the spectrometer mechanically, optically, and finally had focused the spectrometer using Schuster's method. Keeping the spectrometer in the same position, we replaced the Na light by a He-Ne laser source.

First, we tried to find the minimum deviation for distilled water. We allowed the emergent light to fall on a screen. We know angle of deviation changes with the incident angle according to the graph as shown in figure i.e. deviation angle first decreases attains a minimum value and again increases with increase in i. We increased the angle of incidence by rotating the prism table. The point formed by the emergent light moves in particular direction with the rotation of the prism table but at a certain value of the incident angle the point on the screen reverses its direction. This position corresponds to the angle of minimum deviation. We calculated the angle of minimum deviation using spectrometer's vernier scale. The same process was repeated for all the solutions. The solutions were prepared to achieve a particular molarity value. First we prepared in most concentrated solutions with highest molarity. From these solutions we prepared the lower molarity solutions by diluting with distilled water.

3. Results and Discussions

Using the method discussed before, we have calculated the refractive indices of sucrose, copper sulphate and ammonium chloride solutions of different concentrations. The results of the observations are tabulated below.

Table I: Readings for Distilled water

Concentration (water)	Angle of minimum deviation (δ_m) (degree)	Refractive index (μ)
0	22.972	1.325

Table II: Sucrose solution ($C_{12}H_{22}O_{11}$), Molar mass of sucrose – 342 gm

Serial no.	Concentration (molar)	Angle of minimum deviation (δ_m) (degree)	Refractive index (μ)
1	0.050	23.112	1.326
2	0.100	23.441	1.331
3	0.150	23.710	1.334
4	0.211	23.753	1.335
5	0.281	24.289	1.342
6	0.375	24.495	1.344
7	0.500	25.156	1.353

Table III: Ammonium chloride solution (NH_4Cl), Molar mass – 93.5 gm.

Serial no.	Concentration (molar)	Angle of minimum deviation (δ_m) (degree)	Refractive index (μ)
1	0.56	24.135	1.340
2	0.75	25.297	1.350
3	1.00	25.375	1.356
4	1.30	26.196	1.366
5	1.50	27.419	1.382
6	1.70	27.023	1.377
7	2.00	28.294	1.393

Table IV: Copper sulphate solution ($CuSO_4$), Molar mass – 249.7 gm

Serial no.	Concentration (molar)	Angle of minimum deviation (δ_m) (degree)	Refractive index (μ)
1	0.100	23.365	1.330
2	0.150	23.595	1.333
3	0.200	23.365	1.330
4	0.250	23.826	1.336
5	0.300	24.057	1.339
6	0.375	24.134	1.340
7	0.500	24.443	1.344

Graphs between concentration and refractive index are drawn for the three different solutions considered and are shown in Fig (1-3). Data points have been linearly fitted using linear fit program of MATLAB. After doing linear fit to the three graphs, the slopes obtained are listed in Table V. It has been observed that there is a direct relation between the molar concentration of the solution and the refractive index obtained in the experiments. It has been observed that the molar concentration varies as Sucrose > $CuSO_4$ > NH_4Cl and the refractive index obtained from experiments varies as Sucrose > $CuSO_4$ > NH_4Cl.

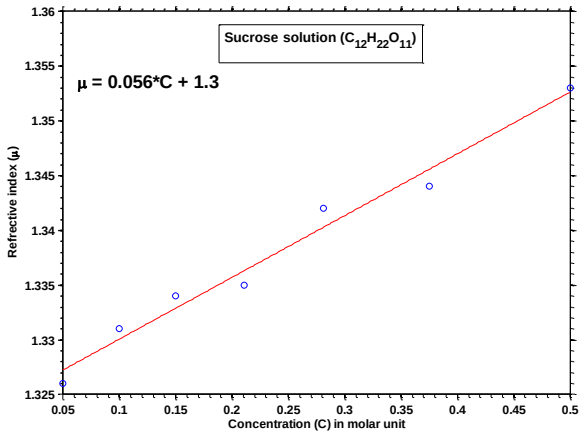

Figure 1: Variation of refrective index with concentration

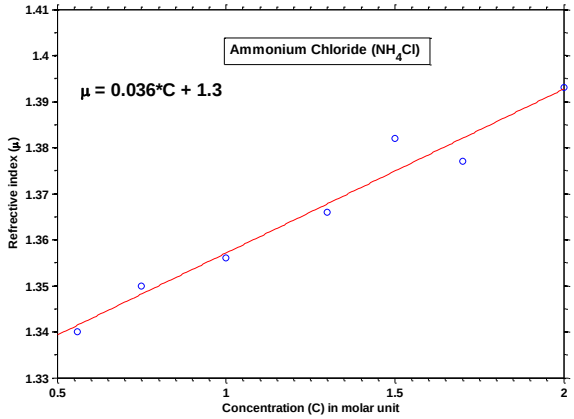

Figure 2: Variation of refrective index with concentration

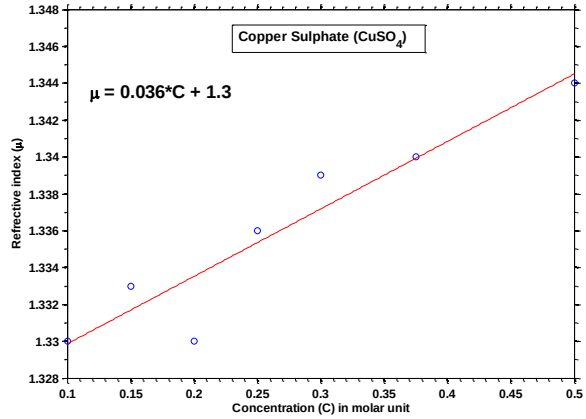

Figure 3: Variation of refrective index with concentration

Table V: Results from graph

Solution	Equation of linear fit	Slope of the graph
Sucrose	μ=0.056xC+1.3	0.056
Ammonium Chloride	μ=0.036xC+1.3	0.036
Copper Sulphate	μ=0.037xC+1.3	0.037

4. Conclusions

We have seen from the results that higher the molar mass of the solute, greater is the slope of the refractive index vs concentration graphs. So, for a certain value of concentration, the refractive index is highest for sucrose and lowest for ammonium chloride. This is because the sucrose molecules are very large as compared to ammonium chloride molecule and it is a branched molecule. So the light wave passing through the sucrose solution interact more with the solute particles than the NH_4Cl solution. So, the refractive index of sucrose solution is higher than that of NH_4Cl solution.

As in our project, we have studied the variation of refractive index of liquid solutions with the concentration dissolve in the liquid at He-Ne laser wavelength 0.6328 μm, we can easily determine the sugar content in common drinks. As a whole, this method is quite capable to determine the solute content dissolved in a solvent which is transparent. It can also be applicable for determination of the content of the other major and minor elements like Ca, Mg, Na and K which directly affects human health.

5. Acknowledgement

The authors would like to thank the Principal, B. Borooah College for his support and also to the head of the Department of Physics for his valuable advice

6. References

[1] Hecht E.,Optics, Pearson Publishing.
[2] Ghatak, A. K., Optics, Tata McGraw Hill
[3] Majumdar, K.G., A textbook on light, Modern Book Agency, Calcutta.
[4] Encyclopedia Britannica.

Bulletin of Physics Projects
Journal homepage: http://www.bbcphysics.in/index.php/journal

Construction of a Variable Electromagnet and Gauss Meter

Tanushree Bezbaruah, Chinmoy Bharadwas, Reinkosi Mam, Barnali Devi, Diganta Kumar Sarma[#]

Department of Physics, B. Borooah College, Ulubari, Guwahati-781007, Assam, India

[#]E-mail address: sarma.diganta@gmail.com

Abstract

This work deals with the construction of varying electromagnet and gauss meter. A simple mechanism is adopted where one can change the current (I) and get varying magnetic field (B). A calibration curve is drawn between B and I. From this graph one can know how much current has to apply to the electromagnet to get a desired value of B. A gauss meter is also constructed using Hall Effect sensor. This gauss meter gives value in terms of Hall voltage (V). Again a calibration curve is drawn between B and V. The value of V for corresponding B can be obtained from this graph. Thus magnetic field B can be measure once we know the Hall voltage. The electromagnet constructed here can produce magnetic field of value about 420 gauss.

1. Introduction

The electromagnet is a type of magnet in which magnetic field is produced by a current. When the current is turned off the magnetic field disappears. Electromagnets are usually consisting of insulated wire wound into a coil. Generally the wire is wound around a magnetic core of ferromagnetic material such as iron. The magnetic field increases due to the presence of the magnetic core.

Danish scientist named Christian Orsted discovered in 1820 that electric currents create magnetic field. British Scientist Willium Sturgeon invented the electromagnet in 1824. His first electromagnet was a horseshoe shaped piece of iron that was wrapped with about 18 turn of bar copper wire. [1]

Scientists have been trying to make powerful electromagnet. In present day the maglab in Tallahassee, Florida holds the record for having the strongest electromagnet of strength 45 tesla. This magnet combines a superconducting magnet of 11.5 tesla with a resistive magnet of 33.5 tesla. It has been operating reliably at 45 tesla since February 2001. The weight and height of this hybrid electromagnet is 31,752 kg and 6.7 meters respectively. Its operating temperature is 1.8 K (i.e. -273^0 C) and required power is 30 MW. [2]

The electromagnets are widely used as components of other electrical devices, such as motors, generators, relays, loudspeakers, hard disk, MRI machines and scientific instruments. Electromagnets are also employed in industry for picking up and moving heavy iron objects such as scrap iron and steel. [1]

Gauss meter is an instrument for measuring the intensity of a magnetic field. Some gauss meters measure the magnitude of the field, and others also measure the direction.

In 1833, Carl Friedrich Gauss, invented the first instrument to measure the magnetic fields. Although he is best known as one of the greatest mathematicians of all time, Carl Friedrich Gauss was also a pioneer in the study of magnetism and electricity. For an extensive survey of terrestrial magnetism, he invented an early type of magnetometer which can measures the directions and strength of a magnetic field. His early magnetometer consisted of a bar magnet suspended in mid-air by a string. While it indicated the direction of the magnetic field, it

offered only a crude measure of the strength. The different types of Gauss meters are-

MODERN GAUSS METER: The modern gauss meters comes in two varieties; scalar meters, which measures just magnitude at a given point and vector meters, which also indicate the direction of the field. Three scalar meters can be aligned to make a vector gauss meter.

HALL EFFECT METERS: The most common gauss meter relies on the Hall Effect, which is a measurable voltage that is produced when a magnetic field across an electrical current. If the current remains the same, then a small change in the magnetic field crosses an electrical current. If the current remains the same, then a small change in the magnetic field produces a similar and predictable change in voltage.

FLUXGATE METERS: Another common gauss meter, known as the fluxgate meter, measures the magnetic field along a given direction. Its main mechanism is two current loops coupled through induction. Multiple fluxgate meters can be used to determine directionality.

PROTON METER: The proton precession magnetometer, or the proton gauss meter, uses nuclear magnetic resonance –the tendency of atoms to absorb and then emit magnetic and electromagnetic energy. The strength of the magnetic field can be measured by the frequency of the atomic excitation. The proton gauss meter is one of the most accurate means of measuring a magnetic field. [3]The main objectives of our project are:

1. To construct a variable electromagnet
2. To construct a Gauss meter using Hall Effect sensor.
3. To draw two calibration graphs between Hall voltage v/s magnetic field strength and current v/s magnetic field strength.

2. Experimental details:

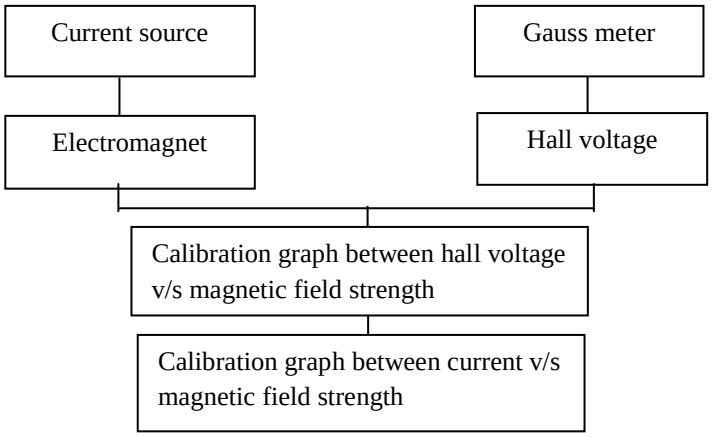

Fig 1: Schematic diagram of the methodology

For the present study the methodology considered is depicted in a schematic diagram (Figure 1). Current from a current source is allowed to flow in the electromagnet which is constructed using copper wire that produces magnetic field. Also using Hall Effect sensor a Gauss meter is developed that will give Hall voltage when placed near a magnetic field. Two calibration curve is drawn between hall voltage and magnetic field and also between current and magnetic field strength.

3. Results and Discussions

3.1 Construction of Electromagnet

The circuit that is used to make the variable electromagnet is shown in the figure2.

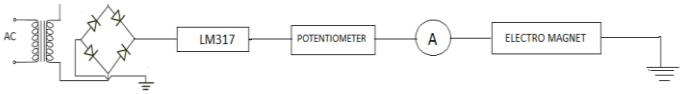

Fig2: Circuit diagram for construction of electromagnet

The description of different components of the circuit is given below:

Transformer: The transformer is used to step down the ac main voltage. We have used transformer having 2050 primary windings and 150 secondary winding so that we get an output voltage of about 13 Volt.

Bridge-rectifier: The bridge-rectifier is used to rectify the ac voltage to dc voltage. The rectifier contains four diodes. Depending on the polarity of the ac voltage, only two diodes in the opposite arm conduct simultaneously, while the other two diodes remain off.

LM317: The LM317 is a popular adjustable linear voltage regulator. It was designed by Robert C Dobkin in 1976 while he worked at National Semiconductor.

Fig 3: Pin position of LM317 IC

The LM317 has three pins Input, output and adjustent. The device is conceptually an opamp with a relatively high output current density. The inverting input of the amplifier is the adjustment pin , while the non-inverting input is set by an internal bandgap voltage refference which produces a stable refference voltage of 1.25 volt. In use an LM317 commonly requires a heat sink to prevent the operating temperature rising too high.[1]

Knob potentiometer: It is a variable resistance. In this project, we have used a potentiometer of range 0 to 100

ohm to vary the current flowing through the electromagnet.

Electromagnet: It is the main part of this project. We have made an electromagnet by winding a copper wire around an iron rod. The strength of an electromagnet is given by the relation:

$$B=\mu \times n \times I$$

where,μ is the permeability of the material of the magnetic core, n is the no. of turns per unit length and I is the current flowing through the wire. So we can change the magnetic field by changing either 'n' or 'I' or both. But to make a strong electromagnet; we must take the magnetic core of higher permeability value. Ferromagnetic materials have higher value of mu. The magnetic domain structure is responsible for the magnetic behaviour of the ferromagnetic materials. A magnetic domain is a region within a magnetic material in which the magnetization is in a uniform direction. This means that the individual magnetic moments of the atoms are aligned with one another and they point in the same direction. When these materials enter a magnetic field, the magnetic domain aligns in the direction of the magnetic field and thus increases the magnetic flux density. Also for ferromagnetic materials have small hysteresis loop area, so the hysteresis loss is minimized. In this project, we have used an iron rod of $\mu = 2.5 \times 10^{-1}$ N/A squared as the magnetic core.

To change the strength of the electromagnet we have changed the current flowing through it using the potentiometer and for different values of current the field strength has measured by using a Gauss meter.

3.2Construction of Gauss Meter:

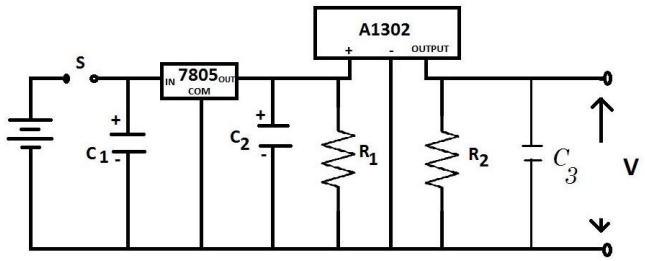

Fig 4: Circuit diagram for the construction of Gauss Meter

The description of different components of the circuit is given below:

LM7805: It is a fixed linear voltage regulator which is used to provide a steady voltage to the circuit.

A1302 Hall-effect device: It is a continuous -time ratio metric linear hall-effect sensor ICs. They are optimized to accurately provide a voltage output that is proportional to an applied magnetic field.

The working principle of Hall Effect sensor is that, when a beam of charged particle passes through a magnetic field, forces act on the particles and the beam is deflected from the straight line. The flow of charged particles through a conductor is known as beam of charged carriers. When a conductor is placed in a magnetic field perpendicular to the direction of the charged particles, they will be deflected from a straight path. As a consequence, one plane of the conductor will become negatively charged and the opposite side will become positively charged. The voltage between these planes is called hall voltage. When force on the charged particles from the electric field balances the force produced by magnetic field, the separation of them will stop. If the current is not changing, then the hall voltage is the measure of magnetic flux density. Since the key factor of sensitivity of Hall Effect sensor is high electron mobility so materials with high electron density is suitable for Hall Effect sensor.

In this project we have used the linear ratio metric Hall Effect sensor A1302. When there is no magnetic field, then the hall voltage should be 2.5 Volt (say V_0). Now, when the electromagnet is brought near the Hall Effect sensor, the voltage reading will change (say V_1) in the voltmeter. If the polarity of the magnet is south, the voltage will increase and decrease when there is North Pole.

The magnetic flux density of electromagnet that we are measuring can be calculated as:

$$B=1000 \times (V_0-V_1)/K\text{Gauss}$$

where K=2.50 milliVolt/Gauss is the sensitivity of Hall device.

3.3 Experimental Data:

The strength of the electromagnet is varied by applying varying current through it and measured the corresponding strength with the help of the Gauss meter.Table I shows the data observed from the constructed electromagnet and Gauss Meter.

3.4 Calibration Curve:

From the Gauss meter, we have got the values of Hall voltage only. So to determine the strength of a magnetic field we have to draw a calibration curve. We have calculated the magnetic strength by using the relation,

$$\mathbf{B= 1000 \times (V_0 - V)/K\ Gauss}$$

and then plotted the value B for different hall voltages in the calibration curve. The graph obtained from the experimental data has been fitted linearly. The equation of the graph is found to be

$$\mathbf{B=770 \times V - 1930}$$

Table I
The variation of strength for different values of Current

Current Applied I (ampere)	Voltage V (in volt)	Magnetic field $B=V_o-V_1$ (in gauss)
0.92	3.07	423.08
0.88	3.05	407.70
0.84	3.03	392.30
0.8	3.01	376.90
0.76	2.99	361.54
0.72	2.97	346.15
0.68	2.96	338.46
0.64	2.93	315.38
0.6	2.9	292.30
0.56	2.88	276.90
0.52	2.85	253.85
0.48	2.83	238.46
0.44	2.81	223.07
0.4	2.79	207.70
0.36	2.77	192.30
0.32	2.74	169.23
0.28	2.72	153.85
0.24	2.69	130.77
0.2	2.67	115.38
0.16	2.65	100.00
0.12	2.62	76.92
0.1	2.61	69.23

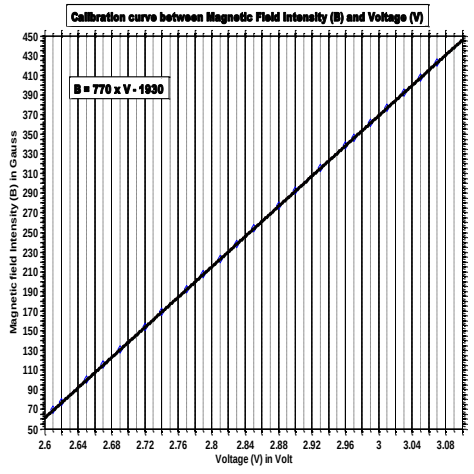

Fig 5: Calibration curve between magnetic field (B) and Hall Voltage (V)

From this calibration curve we are now able to determine the strength of a magnetic field for a particular Hall voltage shown by the gauss meter.

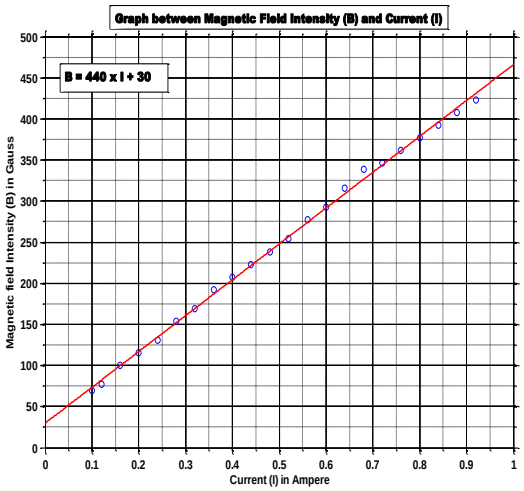

Fig 6: Calibration curve between magnetic field (B) and Current (I)

We further plotted a graph between magnetic strength(B) current(I) (Figure 6). The graph obtained from the experimental data is linearly fitted. The equation of the straight line that we have got can be expressed as:

$$B=440\times I+30$$

From this graph we can determine the strength of a magnetic field for different values of current.

4. Conclusions

This present work is deals with the construction of electromagnet of varying magnetic field. A gauss meter is also constructed that gives the Hall voltage which can be converted to magnetic field using the calibration curve between magnetic field and Hall voltage. The main conclusion of the work is given below.

- We have constructed an electromagnet to produce magnetic field.
- We have varied the magnetic field by changing the current flowing through the electromagnet by using a potentiometer.
- We have constructed a gauss meter to measure magnetic field.
- We tested magnetic field of about 500 gauss.
- A calibration curve is generated between magnetic field strength (B) and hall voltage(V) to calculate B from V.
- We also have generated a calibration curve between current and magnetic field strength.
- The constructed electromagnet can be applied to see the effect of growth of bacteria and seeds.
- Further study will be concentrated towards constructing a high intensity magnetic field.

5. Acknowledgement

The authors would like to thank the Principal, B. Borooah College for his support and also to the head of the Department of Physics for his valuable advice.

6. References

[1] Nave, Carl R. (2012). "Electromagnet", Hyper physics. Dept. of Physics and Astronomy, GeorgiaState Univ. Retrieved September 17, 2014

[2] Intelligent Mechatronic systems: modeling, control and diagnosis.

[3] Electronic control of switched reductance machines

[4] Maglab year report volume 18 No1, spring 2011

[5] googleweblight.com

Bulletin of Physics Projects
Journal homepage: http://www.bbcphysics.in/index.php/journal

Design and development of a LED based Sun-photometer for monitoring atmospheric fluctuations

Dipta S. Mahanta, Mintu Das, Jubin Talukdar, Debabrata Dey and S. Banerjee[#]

Department of Physics, B. Borooah College, Ulubari, Guwahati-7, Assam, India

[#] E-mail address: somikbnrj@gmail.com

Abstract

In the present work, a sun photometer based on LEDs has been designed for monitoring fluctuations in the local atmospheric conditions viz., variations in atmospheric haze and weather conditions on an hourly basis for a period of around fifty days. Data collected using the photometer were primarily used to investigate the attenuation of the direct sunlight after its passage through the atmosphere which provided important information about the atmospheric fluctuations. Results obtained indicate that the atmosphere attenuates for shorter wavelengths (UV) more strongly than longer ones (IR). Attenuation co-efficients for different wavelengths have been determined using Langley plots and the results could also be related physically to the prevalent weather conditions during that time.

1. Introduction

A Sun-photometer is an electronic device specially designed to measure solar irradiance over a narrow range of wavelengths. The concept of handheld Sun-photometer was pioneered by Frederick Volz (1974) and the use of light emitting diodes (LEDs) as detectors of light in such devices was first described by Forrest Mims (1992) [1]. The advantages of using LEDs as detectors are that they are widely available, inexpensive and have a stable optical property. The basic principle behind the use of LEDs as detectors is that they can produce a small photocurrent by absorbing photons which can be amplified by using associated electronics. The most important property of LEDs as detectors is their specificity i.e., each LED is sensitive to a particular wavelength of light; a red LED will produce photocurrent only if red light falls on it and not any other wavelengths. This is true for all other LEDs of different wavelengths.

Sun photometry is an effective technique used to observe fluctuations in the atmosphere. With the help of the photometer, we can detect changes in the attenuation of sunlight over extended periods of time which can be used to discover trends in air quality, weather etc. The transparency of the atmosphere is modulated by aerosols that absorb and scatter sunlight. Increase in the abundance of aerosols decreases the atmosphere's transparency by increasing its optical depth. Optical depth is a dimensionless measure of the attenuation experienced by a direct beam of sunlight during its passage through the atmosphere. Optical depth can be measured with a sun photometer [3-5].

The focus of this work is to observe changes in the attenuation coefficients for different wavelengths of light change over a certain periods of time and associate the data with the prevalent physical fluctuations in the atmosphere during the time of experimentation.

This work revolves around the measurement of the intensity of the sun's rays at various times during the day in order to observe attenuation of the sun rays in the atmosphere. The sun's altitude at the time of data reading should also be noted to calculate the mass number. At midday, the sun hits a maximum altitude with respect to the location of data collection which corresponds to the least thickness of the atmosphere and the air mass in between the photometer and the sun.

The sunlight attenuates in intensity as it travels through the atmosphere, which results in a lower photometer reading than the sunlight's maximum reading at the surface of the atmosphere. However, the intensity of the sunlight at the surface of the atmosphere cannot be directly measured and as such Langley plots have been used. As the sun's placement changes in the sky to lower altitudes, the amount of atmosphere in between the data location and the sun increases. The attenuation of the sunlight follows a decay based on a decay curve of the form,

$$I = I_0 e^{-\lambda M} \quad \text{.....(1)}$$

where, I is the intensity of the incident sunlight on the photometer, I_0 is the intensity value at the surface of the atmosphere; M is the mass number, and λ is the attenuation coefficient.

However, this is a basic form not directly useful for the purposes of the present work. By considering that the mass number is a function of altitude and that the intensity of the sunlight is proportional to the voltage reading displayed on the photometer, Eq. (1) can be rewritten as:

$$V = V_0 e^{-\lambda/\sin\alpha} \quad \text{.....(2)}$$

where, α is the altitude of the sun, V is the voltage reading on the photometer, and V_0 is the voltage reading of the photometer at the surface of the atmosphere mentioned before as the solar extraterrestrial constant. Further manipulation of this equation allows for the Langley extrapolation of these quantities as:

$$\frac{V}{V_0} = e^{-\lambda/\sin\alpha}$$

$$\Rightarrow \ln\frac{V}{V_0} = -\frac{\lambda}{\sin\alpha}$$

$$\Rightarrow \ln V = -\frac{\lambda}{\sin\alpha} + \ln V_0 \quad \text{.....(3)}$$

This form of the equation allows for the indirect measurement of the attenuation coefficient λ as well as the solar extraterrestrial constant given by V_0. By taking voltage data points for the intensity of the sunlight at various times of the day and plotting them against their corresponding sun altitudes α, a Langley plot can be used to measure λ as the slope of a line and the natural log of V_0 as the y-intercept of the plot. This technique has been used to determine the quantities V_0 for each LED frequency as well as observe how the attenuation coefficients for the different frequencies of light would change over the course of time.

2. Experimental Details

2.1. Design of the LED based sun-photometer

The sun photometer consists of an op-amp circuit, two 9V batteries to provide a power source (for the op-amp), a digital voltmeter and a breadboard (cut according to need) to keep an LED light fixed in place. The op-amp component was necessary to amplify the small photocurrent produced in LEDs due to absorption of photons of corresponding frequency for observation and measurement. A digital voltmeter is used to observe the amplified voltage. Figure 1 shows the diagram of the circuit.

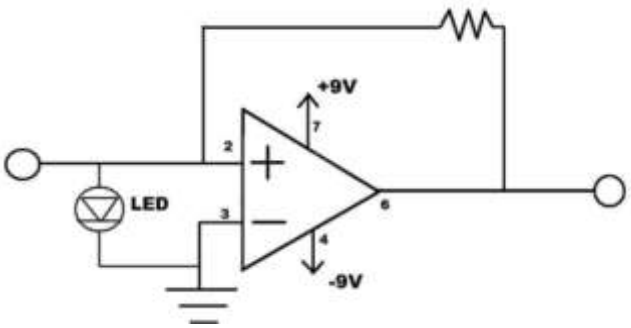

Fig. 1: A diagram depicting the OPAMP circuit used to deliver readable photocurrent

The measured voltage between pin 3 and pin 6 (V_{out}) is collected as data throughout the experiment. The layout of Figure 1 includes the numbered pins at each connection on the 741 op-amp where only the five necessary pins are used. One end of the LED is connected to ground while the other serves as the input voltage (V_{in}) in the op-amp. The amount of amplification depends on the value of the feedback resistance used in the circuit. The feedback resistors used here are 4.7 MΩ, 100 kΩ and 40 kΩ allowing for a voltage gain below the 9V limit of the op-amp. Extra two output ports are made so that a digital multimeter can be connected for taking more accurate readings.

The operational amplifier circuit is connected into a small PCB board and placed into a small box with one freely removable cover for handheld operations. The op-amp used for this photometer is the 741 operational amplifier working at a biasing voltage of 9V supplied by two batteries.

A voltage reading of 0.107 V is present when the photometer LED is enclosed within a dark space. This voltage bias is subtracted from all data points to give the measured values of voltage caused by sunlight intensity. In this manner, the circuit is a current to voltage converter

where the current is driven by the intensity of an LED's response wavelength. The internal circuitry and design of the LED based photometer is shown in the Fig. 2.

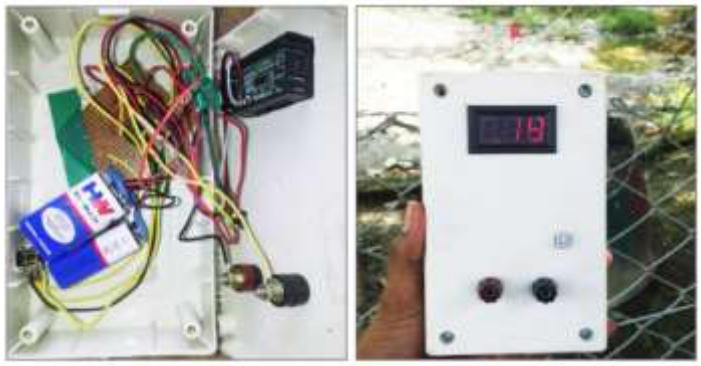

Fig. 2: The self-constructed Sun Photometer designed for the work- Internal circuitry and external view

2.2. Construction of an Astrolabe

In order to measure the solar zenith angle we made an Astrolabe with a protector, a straw and a thread. The straw connected to the protractor is aligned to the direction of the Sun. To make the straw parallel to the sun-rays, we aligned it in such a way that observed circular part was completely illuminated. Then the angle between the thread and the 90^0 line of the protractor is noted down; which is the altitude of the Sun at that time in that place.

2.3. Data acquisition

All data was collected at ground level on the campus of B. Borooah College in Guwahati, Assam (26.178695°N, 91.758007°W) in the month of Feb-March, 2016. The solar zenith angle at any time/date for our location was computed by using an astrolabe.

The work mainly relies on the amount of data taken over a period of time. The experimental data was collected five times a day within an interval of one hour from 1200 hr to 1600 hr repeatedly for 30 days. The result was a series of data sets and plots that show the behavior of the attenuation of sunlight over the course of 30 days. Several LEDs were used in this experiment, each operating at a different wavelength, whose attenuation coefficients and solar extraterrestrial constants were measured.

LEDs of six different wavelengths have been used for the work: Red, Blue, Green, Ultraviolet (UV), Yellow and Infrared (IR) LEDs. When the 4.7 MΩ feedback resistance is used, the voltage output for the Red, Blue, Green and UV LEDs are well below the maximum limit of 9 Volt set by the OPAMP. But the outputs for the Yellow and IR LEDs exceed 9V. Hence, for Yellow and IR readings, 100 kΩ and 40 kΩ feedback resistances have been used respectively, which gave a preferred output below 9V, even in the brightest day. However, for plotting of graphs, the outputs can be manipulated desirably for different feedback resistances. In the course of taking data, the tip of the LEDs was directly aligned to the Sun to take maximum output value. For accurate results, a digital multimeter has been used.

3. Results and Discussions

Employing the data taken for the attenuation of sunlight, Langley plots were generated for each data set for various days. Langley plot is a calibration procedure that relates known changes in atmospheric path length (air mass) with observed changes in signals [2]. Each data set yielded an attenuation coefficient and a value for the solar extraterrestrial constant, corresponding to each day.

3.1. Variation of Voltages

The plots shown in Figures 3 (a-f) are the overall attenuation of the intensity for the six LEDs. From the Fig. 3 (a), we can see that there is a sharp increase of intensity of UV rays over the course of the experiment.The IR plot shown in Fig. 3 (b) depicts a steady increase in intensity over the 30 days which can be associated with the approaching summer season. The increase in intensity will be more sharp and evident if the time period of the experiment would be more.

From the given plots we can see a number of interesting behaviors over the 30 days. Each data set has a different intensity, so the scatter of the data points over the voltage appears greater. Most of the data points show how the different response wavelengths attenuate and have actually changed over the course of the experiment. Since the largest voltage data points coincide to voltage values taken at the highest altitude times, the change in the amount of attenuation between days became apparent. The plots for the attenuation co-efficients for the Blue and Red LEDs [Fig. 3 (c) and (d)] indicate a steady and slow increasing behavior throughout. The Green LED shows a slow and steady increase all the way until the end of the experiment. The Yellow LED plot shows, however, a very interesting result. The readings are low as compared to other LEDs as we used a 40 kΩ resistance in the feedback circuit. Throughout the experiment, the Yellow readings remained almost consistent. With these sets of data, the values for the V_0 and λ are then obtainable.

It is evident from the graphs that the attenuation of different wavelengths of the sun rays after passing through the atmosphere decreases as the voltage readings shows an increasing trend from February to March. This is justified since during February and March we have clear skies with minimum clouds and also there is a transition from winter to summer season which means that the sun rays keep getting intense during this period resulting higher voltages.

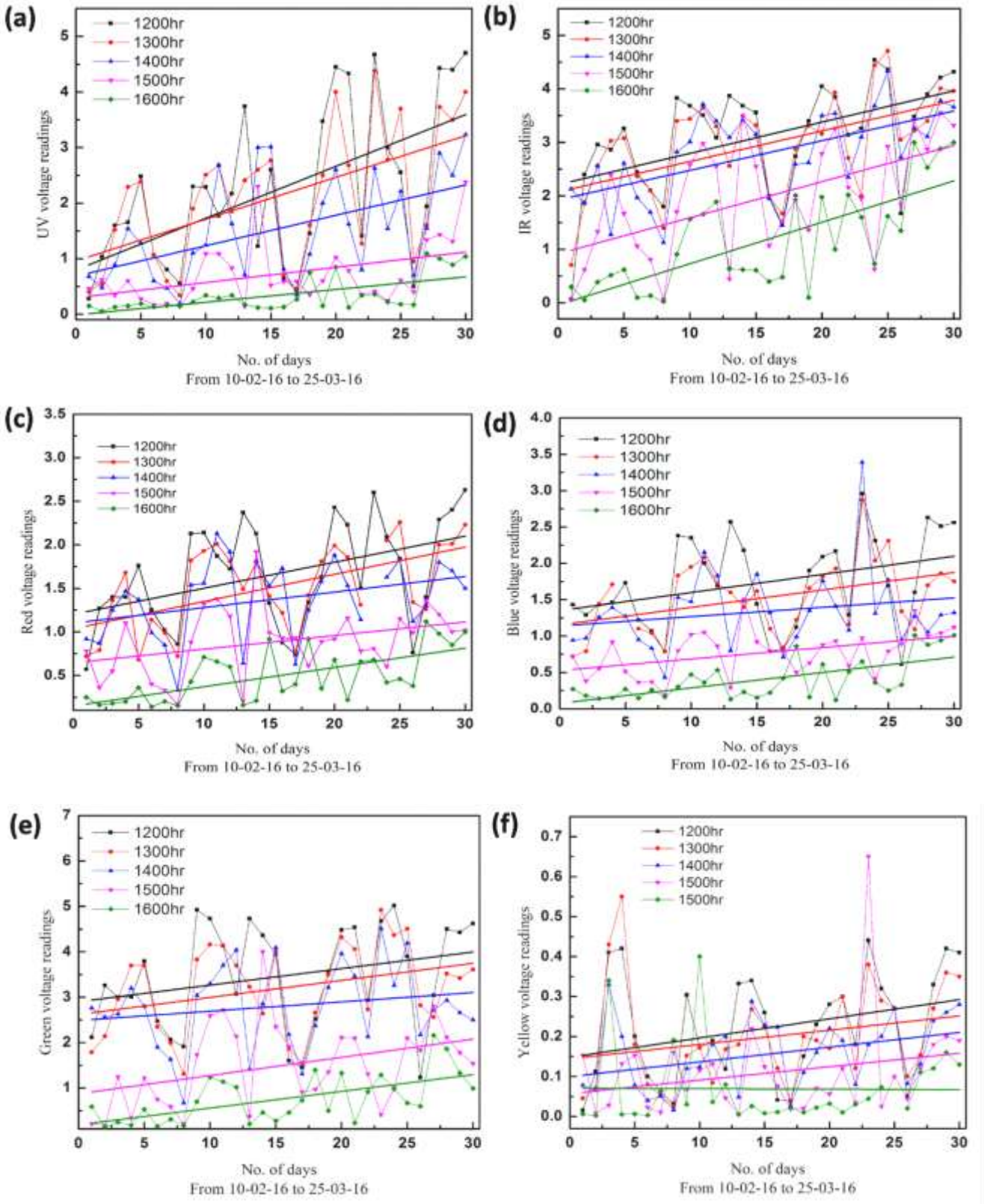

Fig. 3: Variation of voltages collected by the sun-photometer for a period of 30 days from 10-02-16 to 25-03-16 for (a) UV-LED, (b) IR LED, (c) Red LED, (d) Blue LED, (e) Green LED and (f) Yellow LED

3.2. Calculation of V_0 and λ

The attenuation curve shown in the Figure 4 is an example of the curve that each data set taken over a day ideally yields. The mass number varies with the inverse of the sine of the altitude and the expectation was that the light rays attenuate according to the altitude. By taking this decay curve and rearranging it into a Langley plot, the attenuation coefficient λ as well as the value for V_0 were then obtainable for the wavelength.

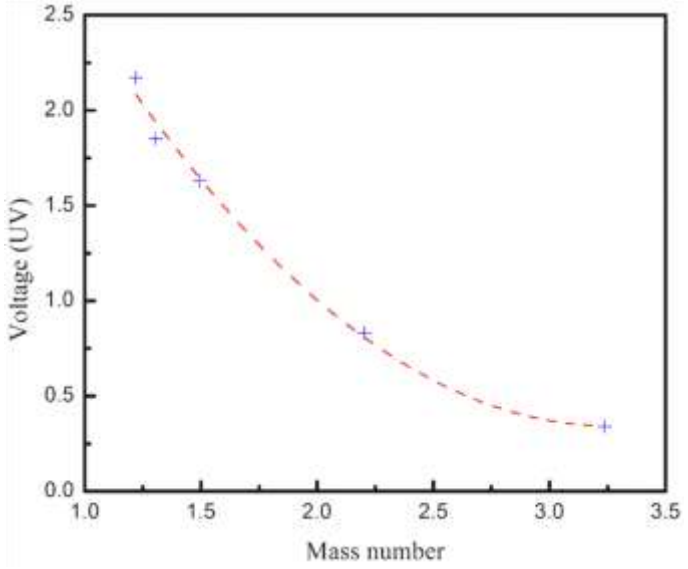

Fig. 4: UV voltage as a function of Mass number

The accompanying Langley plot of the Figure 4 is depicted in Figure 5. By using the fit shown in Figure 5, we are able to determine the coefficient of attenuation as λ = -0.90 and the voltage reading at the top of the atmosphere for UV rays as the value V_0 = 6.23 V.

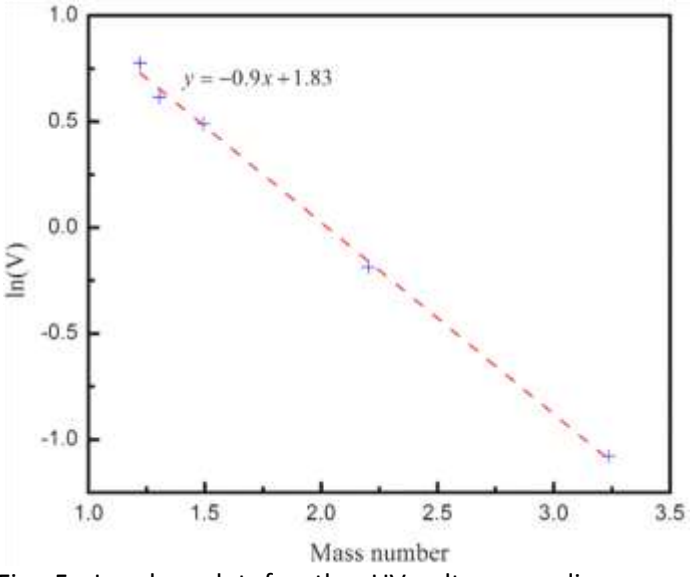

Fig. 5: Langley plot for the UV-voltage readings as a function of mass number

The values for V_0 and λ were then calculated for each day and each wavelength by using the decay curves from these data sets and performing a Langley extrapolation. Each data set yielded a measurement for the solar extraterrestrial constant. The average value of the calculated constant along with the standard deviation for the measurements is tabulated in Table 1.

Table 1: Average Value of V_0 determined from Langley plots of each experimental day

Colour	V_0
Red	1.16 ± 0.55
Blue	1.32 ± 0.66
Green	2.10 ± 0.62
UV	1.54 ± 0.66
Yellow	0.60 ± 0.20
IR	1.90 ± 0.88

3.3. Variation of attenuation co-efficients

Each day yielded a unique attenuation coefficient, and in a similar manner, we were able to find how the sunlight attenuated with respect to the amount of atmosphere and the time of day. On the same time scale, the attenuation coefficients are plotted with respect to the number of days in figures 6 (a-f) for the different wavelengths.

Figure 6(a) shows the attenuation coefficients for the UV LED. The mean reading of the attenuation coefficient is λ=0.933 for the sunlight of wavelength 280-400 nm. The readings are widely varying for UV as seen in the graph. Figure 6(b) shows the attenuation coefficient variation for IR LED. It is clearly evident from the graph that the attenuation coefficient for IR is decreasing throughout the experiment. Two or three outlier points in the graph indicate an extreme variation in the weather. The decreasing pattern of the graph is because of the approaching summer season while conducting the experiment. The mean value of the attenuation coefficient for IR centers around λ=0.655 for the sunlight of wavelength 700nm-1mm. The attenuation coefficient variation is plotted in Figure 6(c) for Red LED. It shows a steady decrease in λ. The mean of the attenuation coefficient for Red is λ=0.66 for the sunlight of wavelength 620-750 nm. However, some values of λ appeared very low in the later days which may be accounted for the extreme weather conditions. The attenuation coefficients for Blue, Green and Yellow LEDs are plotted above in Figure 6 (d-f). The deviation of the attenuation coefficients from the mean value λ=0.741 for the sunlight of wavelength 450-495 nm is more visible for the Blue LED readings. However, an overall decrease in λ is evident from the plotting.

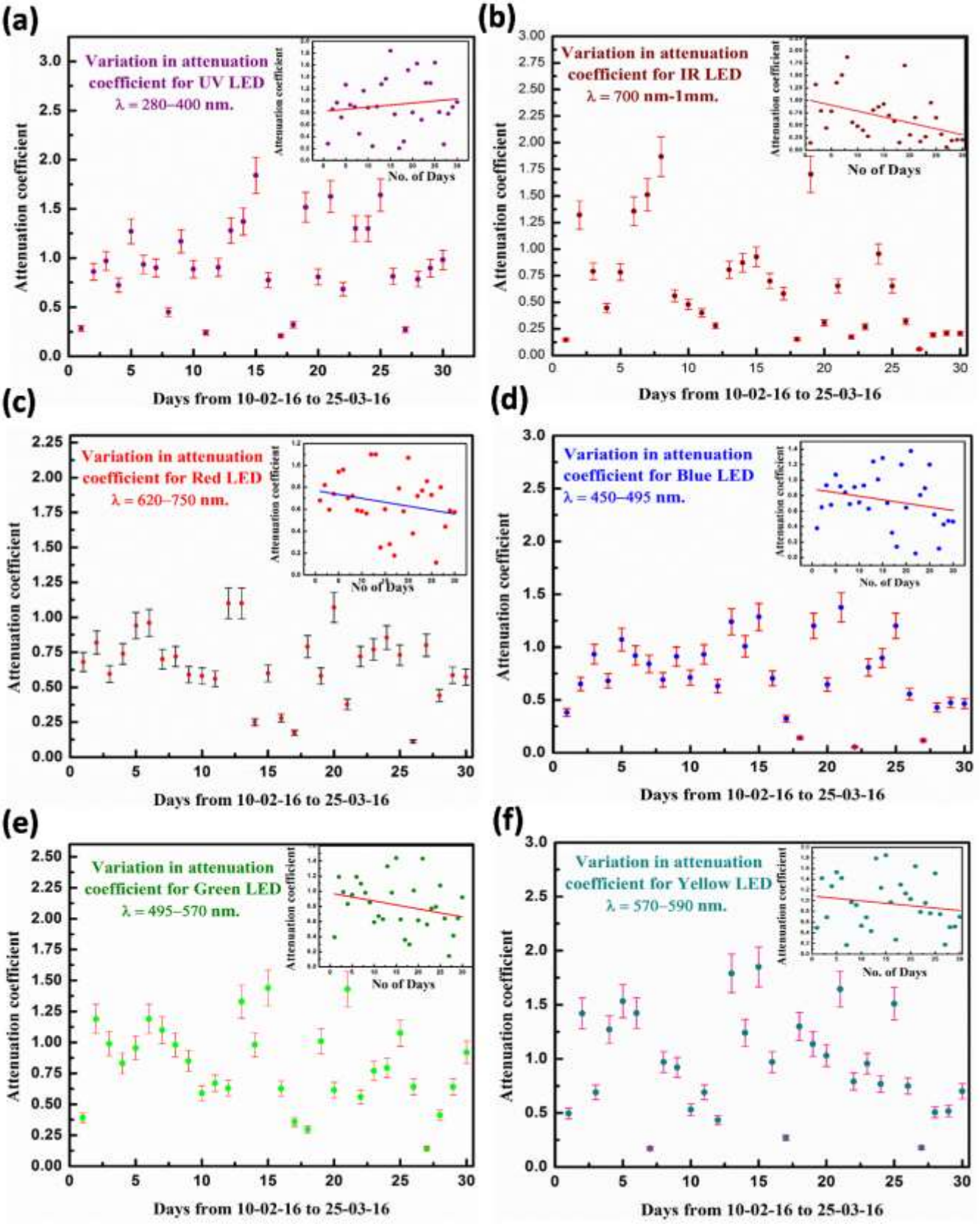

Fig. 6: Variation of attenuation co-efficient as a function of number of days for (a) UV-LED, (b) IR LED, (c) Red LED, (d) Blue LED, (e) Green LED and (f) Yellow LED

In case of Green LED, the points are somehow condensed relatively more than the Yellow LED. The mean value of the attenuation coefficient for Green (wavelength 495-570 nm) is λ=0.813 and for Yellow (wavelength 570-590 nm) is λ=0.948.

4. Conclusions

The original goal of the work by Mims, 1992 was to develop a family of inexpensive, accurate LED Sun photometers for the measurement of aerosol optical thickness (AOT) and total column water vapor. [3, 4] The results presented here demonstrate the monitoring of the weather conditions. The LED sun photometer we constructed is much more portable and less costly than the other instruments with similar goals. Therefore, it is reasonable to conclude that the LED sun photometer method is appropriate for measuring both short-term and long-term trends in weather change.

In our project, having taken periodic data, the long term behavior of the sunlight as well as attenuation of sunlight for different wavelengths became much clearer. From the Figures, we can conclude that the atmosphere attenuates for shorter wavelengths (UV) more strongly than longer ones (IR). A fix that could be made to minimize the margin of error present in some of the plots could be in the using of LEDs with smaller response wavelength curves. Also, choosing a more clear weather time of the year to take data such as spring and summer rather than fall and winter would eliminate many outlier points and allow for more frequent data taking than was sometimes possible.

5. Acknowledgement

The authors would like to thank the Head, Department of Physics and all the faculty members for their constant encouragement, useful discussions and support during the work.

6. References

[1]. Journal of geophysical research, Vol. 106, No. D5, Page-4733-4740, March 16, 2001.

[2]. http://www.ncbi.nlm.nih.gov/pmc/articles/PMC3885532/

[3]. Mims, F. M., III, Sun photometer with light-emitting diodes as spectrally selective detectors, Applied Optics, 31, 6965-6967, 1992.

[4]. Mims, F. M., III, How to Monitor Ultraviolet Radiation from the sun, Scientific American, 263(2), 106-109, August 1990.

[5] 'Atmosphere Observation by the Method of LED Sun Photometry' by Gregory Garza; Physics Department, California Polytechnic State University, San Luis Obispo; April, 2013.

Bulletin of Physics Projects
Journal homepage: http://www.bbcphysics.in/index.php/journal

Properties of transition metal doped carbon nanotubes: a theoretical study

Samir Thakur [1], Dilip Saikia[3], Pratidutta Sen[3], Rehana Khatoon[3], Debajit Saikia[4], Nirab C. Adhikary[2#]

[1]Department of Applied Sciences, Gauhati University, Guwahati-781014, Assam, India
[2]Physical Sciences Division, Institute of Advanced Study in Science Technology, Paschim Boragaon, Gorchuk, Guwahati-781035, Assam, India
[3]Department of Physics, Handique Girls' College, Dighali Pukhuri West, Guwahati, 781001, Assam, India
[4]Department of Physics, Moridhal College, Moridhal, Dhemaji, 787057, Assam, India

[#]Corresponding author's e-mail address: nirab.physics@gmail.com

Abstract

In this paper, we investigated the structural properties of Scandium (Sc) and Titanium (Ti) doped single wall carbon nanotubes (SWCNTs) using density functional theory. The doping is done on the external wall of the carbon nanotube. Our theoretical calculation shows that doping significantly affects the geometrical structure of the carbon surface. The structural optimization shows that the doping not only modifies the bonding arrangement of the neighboring carbon atoms but also introduces a planner distortion. From the simulated Density of states spectrum, it is found that the energy gap decreases when the dopant changes from Scandium (Sc) to Titanium (Ti) in the same row of the periodic table. Moreover, the Shift of the Fermi energy level also has been observed. The detailed simulation has been discussed thoroughly by using the natural bond orbital analysis, frontier molecular orbitals, partial charge distribution and the electrostatic potential surfaces.

1. Introduction

Carbon nanotube (CNT) is the name of ultrathin carbon fiber with nanometer- size diameter and micrometer-size length and was first discovered by a Japanese scientist, Sumiolijima [1]. The structure of CNT consists of enrolled graphitic sheet and can be classified into either multi-walled or single-walled CNT (MWCNT or SWCNT) depending on its preparation method. CNT is the material lying in-between fullerenes and graphite as a quite new member of carbon allotropes. It seems that a considerable number of researchers have been participating in the science of CNTs and there has been a remarkable improvement in the both experimental and theoretical studies on MWCNT and SWCNT particularly during the last couple of years. As per as the application is concern it is found that CNTs has got most active area of research in the past few decades due to their attractive mechanical, thermal, and electrical properties and various applications, including hydrogen storage[2], chemical sensors [3], and Nano bioelectronics[4], etc. Nowadays

scientists trying to enhance these properties of carbon nanotubes by incorporating different doping elements. Chen et al [5] investigated the properties of transition-metal-doped single-walled carbon nanotubes (SWCNTs) using density functional theory and found that when the dopant changed from Sc to Zn in the same row of the periodic table and from top to the bottom in the same Pt group, the energy of the highest occupied molecular orbital of the transition metal-doped SWCNTs decreases, which indicates reduced electron donating ability. Buzatu et al [6] manipulated the molecular orbital energy gap (HOMO-LUMO gap) of the nanotubes by incorporating transition metal as the doping elements. They also demonstrated that multiple metal filled nanotubes could be used to construct a molecular nanotube based transistor. Dhibar et al [7] found that transition metal doping on SWCNTs will enhance its electrochemical properties of the nanocomposites which result better specific capacitance and charge/discharge rates makes them promising candidates as electrodes in super capacitors. However detailed theoretical analysis of Sc and Ti doped SWCTs haven't found yet. In this work the effect of Sc and Ti doping on the external surface of the carbon nanotubes have been studied using natural bonding orbital analysis, Density of states, partial charge distribution, electrostatic potential, frontier molecular orbitals etc.

2. Computational Methods

The density functional theory has been applied for performing the computational simulation under Gaussian 09 software package[8].The PBEPBE exchange correlation functional is used which was developed by Predew, Burke and Ernzohoff [9] along with the Lanl2DZ basis set. The reason for choosing the above mentioned computational scheme is that it has already been used by other researchers for the analysis of transition metals and carbon interaction [5].

An armchair (5,5) SWCNT structure is designed which consists of 100 atoms, out of those 80 atoms are carbon and 20 atoms are hydrogen. In the simulation, hydrogen atoms are added so as to avoid the dangling bonds of the SWCNT boundary and no edge effect is considered.

The geometry optimization of the undoped carbon nanotube is performed without any symmetry constraint. After that, the frequency calculation (normal mode analysis) is carried out so as to get the true optimized CNT structure. Now to get the doped CNT structure one carbon atom of the undoped carbon surface has been replaced by the dopant atom and again structure optimization has been done.

3. Results and Discussions

To obtain the most energetically favorable Sc and Ti-doped CNT structures, we considered a particular site on the carbon surface as shown in Figure 1(a).Structural distortions occur to the external wall of carbon surface when Sc and Ti used as a dopant. The Sc-C bond (~2.07 Å) is longer than compare to that of Ti-C(1.92 Å) and pristine SWCNT (1.44 Å).The angle between Sc and neighboring carbon, in Sc-doped CNT is found to be ~850 which is less than compare to the bond angle of carbon on the carbon surface. As a result, the position of the Sc in the doped CNT is shifted upwards. Similarly, the position of Ti is also shifted upwards and the angle between Ti and neighboring carbon is found to be ~900. The above result shows that both Sc and Ti individually effect the local bonding environment of carbon nanotube due to their difference in covalent radii (144 pm and 136 pm Sc and Ti respectively) and electro negativities (1.36 and 1.54, Sc and Ti respectively) Because of this reason both Sc and Ti cause significant planar distortion in CNTs.

The frontier molecular orbitals are significant while understanding chemical reactivity. We have shown the highest occupied molecular orbitals (HOMOs) and lowest unoccupied molecular orbitals (LUMOs) in Figure 1. When the dopant changes from Sc to Ti, It is found that the HOMO energy, along with the electron donating ability, decreases from -3.85 eV to - 4.02 eV.

The geometrical parameters can be found in Table 1. Natural bonding orbital analysis shows that there is no C-Scbond exist after doping in the case of Sc-doped CNT. However, the existence of C-Ti bond found in the case of Ti-doped CNT. The natural bond orbital type is recorded in the following Table 2 and Table 3.

Table 1: The length of bonds in Å (5, 5) CNT systems

Sample Code	C1-X	C2-X	C3-X
Pristine	1.44	1.44	1.43
Sc-CNT	2.08	2.07	2.11
Ti-CNT	1.97	1.92	1.96

Table 2: Natural bonding orbital analysis of Ti doped SWCNT system.

Natural Bonding orbital	Occupancy	Composition
C1 – Ti	0.89549	66.26 % C1 $sp^{2.65}$+ 33.74% Ti $spd^{2.33}$
C2 – Ti	0.93593	65.68% C2 $sp^{2.5}$ + 34.32% Ti $spd^{2.59}$
C3 - Ti	0.93909	67.68 % C3 $sp^{2.61}$ + 32.32% Ti $spd^{2.35}$

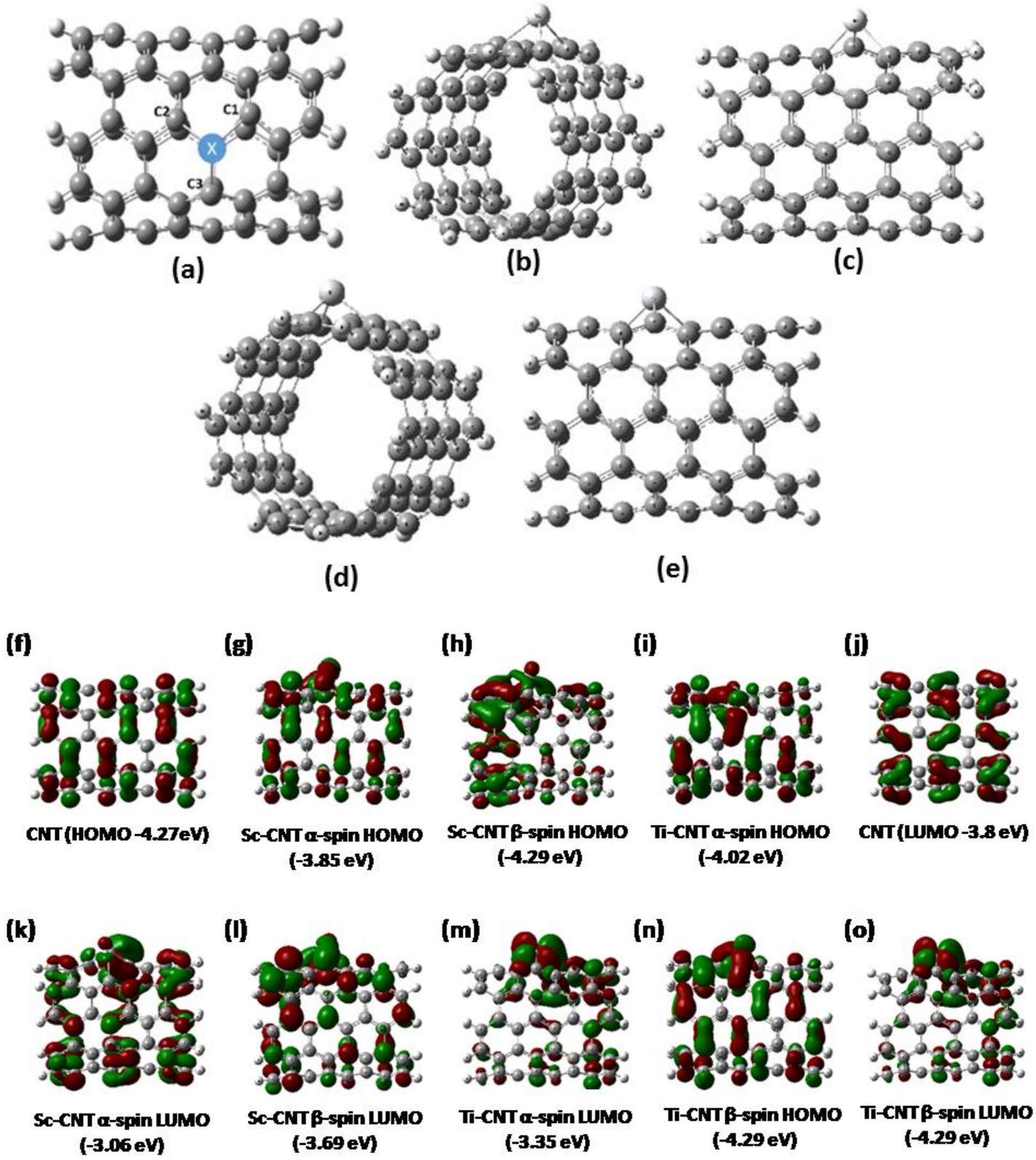

Fig. 1: The doping site and frontier orbitals of the pristine, Sc- and Ti-doped SWCNTs. Orbital energies (in eV) are shown in Parentheses

Table 3: Natural bonding orbital analysis of the pristine SWCNT.

Natural Bonding orbital	Occupancy	Composition
C2-C	1.95841	49.71%C2 $sp^{2.08}$ + 50.29% C $sp^{2.08}$
C3-C	1.96007	50.51%C3 $sp^{1.91}$ + 49.49% C $sp^{2.10}$
C1-C	1.94509	50.01%C1 $sp^{2.28}$ + 49.99% C $sp^{2.28}$

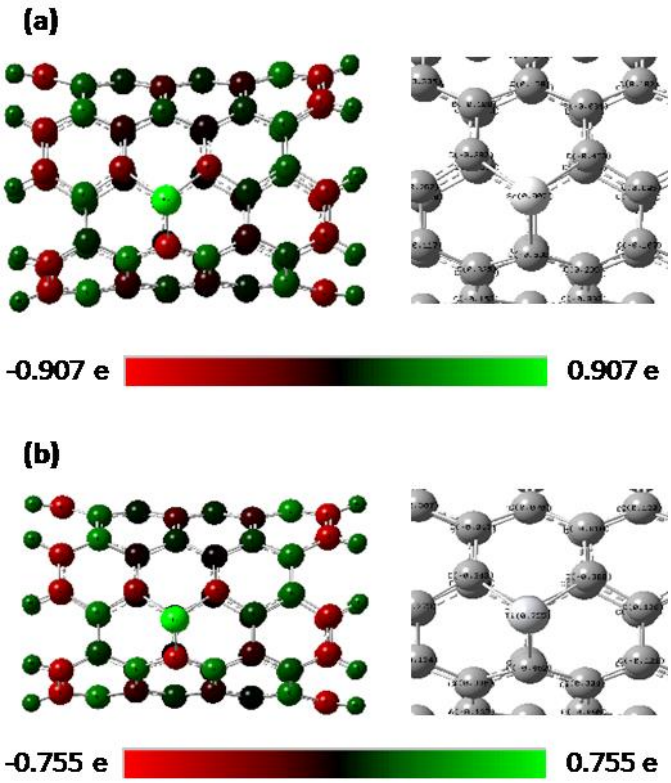

Fig. 2: Schematic illustration of the model (5, 5) pristine SWCNT with partial charge distribution

The partial charge distribution in Figure 2 shows that Sc transfers -0.382e, -0.420e and -0.538e charge to its nearest neighbour carbon atoms. Similarly, Ti transfers -0.343e, -0.388e and -0.462e charge to its nearest neighbour carbon. It can be explained in the following way, the metallic character decreases from the left to the right in the same row of the Periodic table. Since Sc present at the left-hand side of the periodic table than comparing to Ti, so it transfers more negative charges to its neighbouring C atoms. Because of this reason Sc has got more positive charge compared to Ti. The values of partial charges are scaled according to the colored bar at the bottom. The color green indicates a positive charge and the color red, a negative charge. Darker the color (red or green), larger the magnitude of the partial charge on the atom.

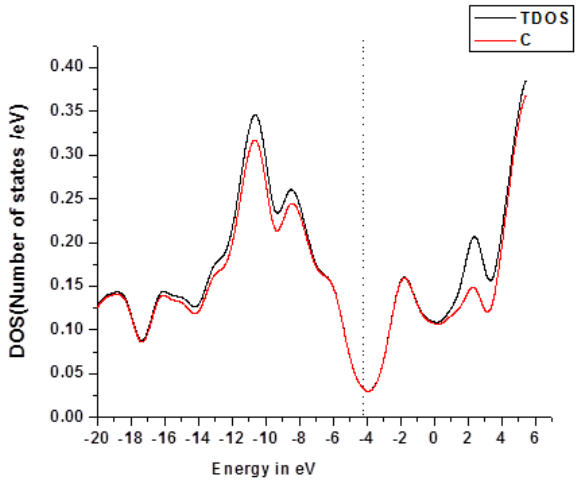

(a)Pristine CNT (Fermi energy $E_{F\ alpha}$= - 4.27eV)

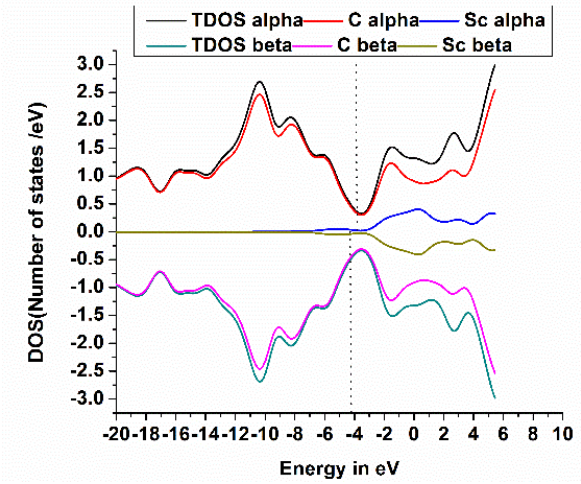

(b) Sc-CNT ($E_{F\ alpha}$= - 3.85 eV and $E_{F\ beta}$= -4.29 eV)

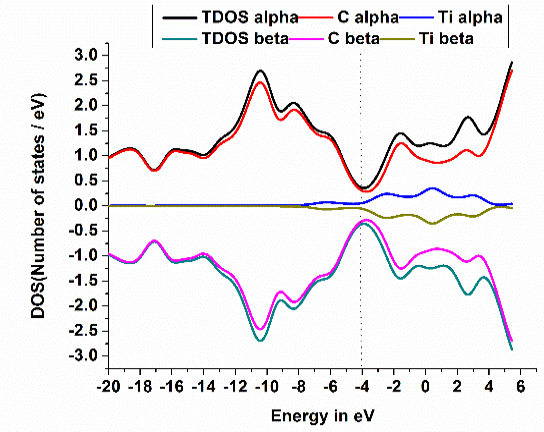

(c) Ti-CNT ($E_{F\ alpha}$= - 4.01 eV and $E_{F\ beta}$= -4.01 eV)

Fig. 3: Density of states (DOS) of the pristine, Sc- and Ti-doped(5,5) SWCNTs.The DOS of α –spin and β-spin electrons are shown in the upper and lower panels,respectively. Fermi levels are marked by the vertical dotted lines.

In Figure 3 it is found that the partial density of states (PDOS) of Sc-doped CNT near the Fermi level go through significance changes the Fermi energy level shifted from -4.27 eV to higher energy -3.85 eV, but in case of Ti doped CNT the Fermi energy level shifted from -4.27 eV to higher energy -4.01 eV. Thus the result shows that Sc-doped CNTs are better electron donor compare to Ti doped CNTs.

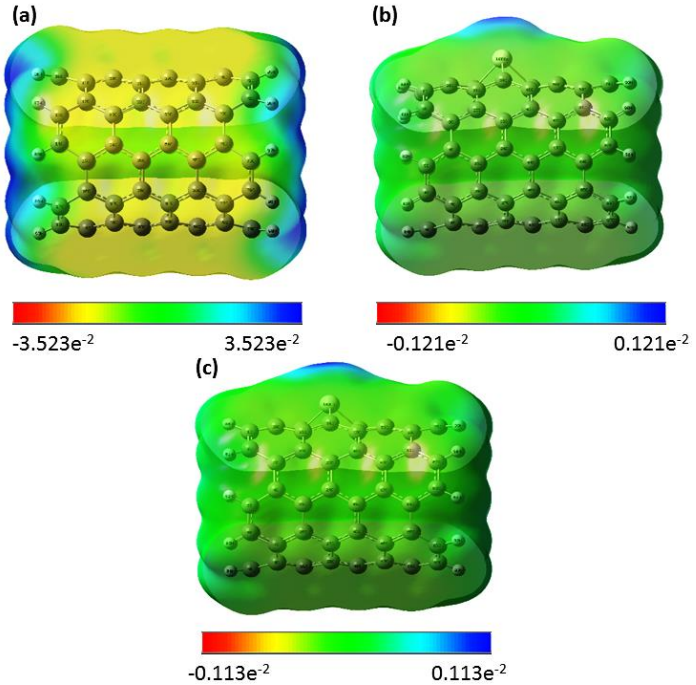

Figure 4: .Molecular electrostatic potential surface of (a) Pristine CNT (b) Sc doped CNT and (c) Ti doped CNT

Molecular electrostatic potential at a point in space around a molecule gives information about the net electrostatic effect produces at that point by total charge distribution of the molecule and correlates with dipole moments, electronegativity, partial charges and chemical reactivity of the molecules. It provides visual method to understand the relative polarity of the molecule. The distribution of electrostatic potential is shown in Figure 4 as a color overlay. Here, the values are scaled according to the colored bar at the bottom. The color blue indicates more positive portion and from yellow, to red it indicates the more negative portion of the potential surface. Such mapped electrostatic potential surface has been plotted for pristine, Sc and Ti-doped SWCNTs using the software Gauss view. The pristine carbon nanotube is found to be weakly positive on most of the outer and inner surfaces, but it is strongly positive at the two ends of the carbon nanotubes due to the presence of hydrogen.

In this case hydrogens at the carbon nanotube ends act as charge donors. Moreover, the magnitudes of both the positive and negative surface potentials associated with the basic carbon tend to be larger where the curvature is greater. However, in the case of Sc and Ti-doped CNT structures, the surface potential becomes neutral.

4. Conclusions

Density functional theory (DFT) has been employed to investigate the doping of Sc and Ti on CNT surface. Results obtained from the present study shows that there is a decreasing electron donating ability as well as decreasing HOMO-LUMO energy gap from 0.78eV to 0.67 eV when the dopant changes from Sc to Ti in the same row of the periodic table. The lowering of HOMO-LUMO energy gap supports bioactive property of the molecule. The study of potential energy surface shows that by changing the different doping elements tubes can be designed with potential patterns tailored to specific objectives. This encouraging result could be of interest to enhance further theoretical research relaying on the experimental evidence and vice versa.

5. Acknowledgement

The authors would like to thank the Physical Science Division, Institute of Advance Study in Science and Technology (IASST) for providing the computing facility.

6. References

[1] S. Iijima, Nature. 354 (1991) 56-58.

[2] C. Liu, Y. Y. Fan, M. Liu, H. T. Cong, H. M. Cheng, M. S. Dresselhaus; Science. 286 (1999) 1127.

[3] J. Kong, N. R. Franklin, C. W. Zhou, M. G. Chapline, S. Peng, K. J. Cho, H. J. Dai; Science. 287 (2000) 622.

[4] E. Katz, I. Willner; ChemPhys Chem. 5 (2004)1085.

[5] Y. K. Chen, L. V. Liu, W. Q. Tian, and Y. A. Wang; J. Phys. Chem. C.115 (2011) 9306–931.

[6] D. A. Buzatu, F. T. Nguyen, S. N. Reddy and J. A. Darsey; J. Comput. Theor.Nanosci.l (2004) 1-7.

[7] Saptarshi Dhibar, Pallab Bhattacharya, GoutamHatui, Sumanta Sahoo, and C. K. Das. ACS Sustainable Chem. Eng.2 (2014)1114−1127.

[8] M. J. Frisch, G. W. Trucks, H. B. Schlegel, G. E. Scuseria, M.A. Robb, J. R. Cheeseman, G. Scalmani, V. Barone, B. Men-nucci, G. A. Petersson, H. Nakatsuji, M. Caricato, X. Li, H.P. Hratchian, A. F. Izmaylov, J. Bloino, G. Zheng, J. L. Sonnenberg, M. Hada, M. Ehara, K. Toyota, R. Fukuda, J. Hasegawa, M.Ishida, T. Nakajima, Y. Honda, O. Kitao, H. Nakai, T. Vreven, J.A. Montgomery, Jr., J. E. Peralta, F. Ogliaro, M. Bearpark, J.J. Heyd, E. Brothers, K. N. Kudin, V. N. Staroverov, R.Kobayashi, J. Normand, K. Raghavachari, A. Rendell, J. C. Burant, S. S. Iyengar, J. Tomasi, M. Cossi, N. Rega, J. M. Millam, M. Klene, J. E. Knox, J. B. Cross, V. Bakken, C. Adamo, J.Jaramillo, R. Gomperts, R. E. Stratmann, O. Yazyev, A.J. Austin, R.

Cammi, C. Pomelli, J. W. Ochterski, R. L. Martin,K. Morokuma, V. G. Zakrzewski, G. A. Voth, P. Salvador, J.J. Dannenberg, S. Dapprich, A. D. Daniels, O. Farkas, J.B. Foresman, J. V. Ortiz, J. Cioslowski, D. J. Fox, Gaussian 09, Revision A.01, Gaussian, Inc., Wallingford CT (2009).

[9] J. P. Perdew, K. Burke, M. Ernzerhof; Phys Rev Lett. 77 (1996) 3865–3868.

Bulletin of Physics Projects
Journal homepage: http://www.bbcphysics.in/index.php/journal

Design and Calibration of a LED based digital colorimeter for determination of unknown concentrations of $CuSO_4$ and $K_2Cr_2O_7$ in aqueous solutions

Nitul Malakar, Kapinjal Talukdar, Bimugdha Goswami, Chintu Moni Deka and S. Banerjee[#]

Department of Physics, B. Borooah College, Ulubari, Guwahati-781001, Assam, India

[#]Corresponding author's e-mail address: somikbnrj@gmail.com

Abstract

In this paper, we have designed and calibrated a LED based digital colorimeter for determination of unknown concentrations of some inorganic compounds viz., Copper Sulphate ($CuSO_4$) and Potassium dichromate ($K_2Cr_2O_7$) in aqueous solutions. The results obtained for $K_2Cr_2O_7$ depicts linear behavior within the concentration range of 0.01 to 0.14 M. However, it was observed that for the $CuSO_4$ solution, the graph could be divided into two different concentration regimes. The behavior was found to be linear for low concentrations upto 1.0 M while for concentrations higher than that the slope of the graph increased. Overall behavior was however found to be non-linear for $CuSO_4$.

1. Introduction

Colorimeters are photometric instruments that can be used to measure the concentration of organic and inorganic compounds in a solution by determining the absorbance of specific wavelengths of lights in such compounds. Colorimeter can be used to develop a profile of the sample rather than just simple detection of the presence of a chemical compound. Being a light sensitive device, a colorimeter can measure transmittance and absorbance of light passing through a liquid sample. The device measures the intensity or concentration of the color that develops upon introducing a specific reagent into the solution. When we allow white light, consisting of different wavelengths of light corresponding to different color, to fall on a test solution one color or a band of wavelength is absorbed depending solely on the type of compound used. The ions present in the solution determine the absorbed wavelength. Different chemical substances absorb different wavelengths of light in the visible range. However, the amount of light absorbed or transmitted depends on the concentration of that compound present in the solution. Since colorimeters are generally used for testing for a single ion, the wavelength of light that is passed through the test solution is selected either by using color filters or by the use of specific wavelength of light in order to identify that particular ion.

A colorimeter consists of the following main components: (a) a light source which acts as the input, (b) a cuvette in which organic or inorganic solvent is placed for allowing the light to pass through and (c) a detector which can detect the transmitted light after absorption and convert it into electrical output.

The basic principle behind the working of a colorimeter is the Beer-Lambert's law, according to which the absorption of light transmitted through a medium is directly proportional to the concentration of the medium. Beer's law is an equation that relates the attenuation of light to the properties of a material. Actually, the law is the linear relationship between absorbance and concentration of an absorbing species. The law states that the concentration of a chemical is directly proportional to the absorbance of a solution. This relation may be used to determine the concentration of a chemical species in a solution using a colorimeter or spectrophotometer. But, Beer's law is not valid at high solution concentrations. Also the absorbance is directly proportional to the length of the light. The general Beer-Lambert law is usually written as [1]:

$$A = a(\lambda) \times b \times c \quad \ldots\ldots\ldots\ldots\ldots\ldots\ldots\ldots\ldots\ldots(1)$$

where, A is the measured absorbance, $a(\lambda)$ is a wavelength dependent absorptivity co-efficient, b is the path length and c is the concentration of the analyte used [1].

The linearity of Beer- Lambert law is limited by several factors such as scattering of light due to particulates in the sample, fluorescence or phosphorescence of the sample or variations in chemical equilibrium as a function of concentration. Moreover, this law is not valid for very high concentrations [1].

2. Experimental details

2.1. Circuit design and instrumentation

The circuit diagram used for fabricating the colorimeter is shown in the Fig. 1.

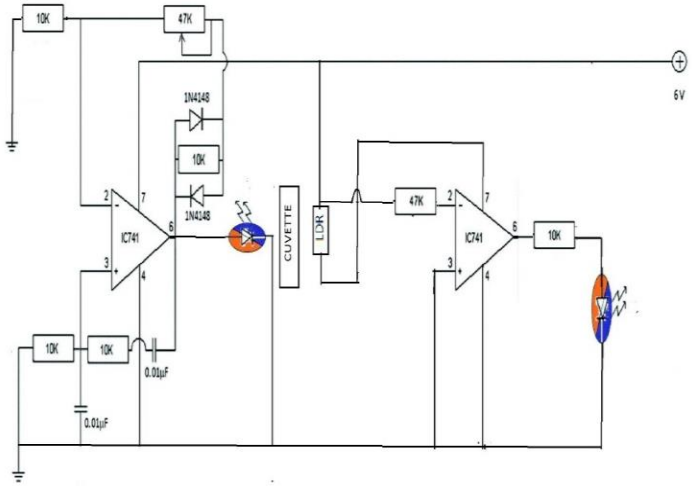

Fig. 1: Circuit design for the device

Two OPAMP circuits have been used to construct the colorimeter for our experiment. The 1st circuit is an IC741 OPAMP circuit. In this circuit a portion of the biasing voltage is given to the input by a feedback loop. The input signal is then converted into an amplified signal and hence we get an amplified output across which an LED is connected. This LED acts as the source light for the solution. The 2nd circuit is also an IC741 OPAMP circuit which acts as the light detector circuit. An LDR (light detecting resistance) is connected to the input biasing signal and a portion of the biasing signal is given to the input. Now when the light, transmitted from the solution falls on the LDR its resistance changes and we get different output voltages.

To construct the instrument, the two circuits were placed in two opposing walls of a plastic box so that the LED and the LDR falls in a line in front of each other. In between the two circuits arrangements are made to place the cuvette which allows the light beam from the LED to travel through the solution in the cuvette. The LED and the LDR are covered with two black colored pipes to make sure that whole of the input light from LED falls on the solution and whole transmitted light falls on the head of the LDR. This arrangement minimizes the chance of scattering of light

2.2. Methodology

In order to perform the present work, we adopted the following methodology. Two inorganic compounds copper sulphate ($CuSO_4.5H_2O$) and Potassium Dichromate ($K_2Cr_2O_7$) were taken as our test sample. Solutions of different concentrations of copper sulphate were made taking distilled water as solvent. A small amount of the solution of a particular concentration is taken in a cuvette and placed in front of the input light beam. As the beam travels through the solution, some part of the light gets absorbed and the remaining falls on the LDR (Light Dependent Resistor). Due to this the resistance of the LDR decreases and hence allows current to flow through the circuit and we get an output voltage in the voltmeter and the digital multimeter. The voltage reading for direct beam and transmitted beam for each solution of different concentration were noted down. The same process was followed for $K_2Cr_2O_7$.

3. Results and Discussions

Table 1 depicts the data obtained for the experiment using the colorimeter for $K_2Cr_2O_7$. Using these values a graph has been plotted and is shown in Fig. 2 taking Molarity (M) along X-axis and the differential output voltage (V) along Y-axis. The differential output voltage refers to the difference between the direct voltage reading without the solution and the voltage readings obtained after light is absorbed in the solution. The data points obtained were plotted in the form of a calibration graph for potassium dichromate using which any unknown concentration of potassium dichromate can be determined. Two curves were drawn and compared, one for the reading

from the inbuilt voltmeter (A) and other from the reading from external digital multimeter (B).

Slope of the graph (from A) = $\frac{2.44-1.52}{0.14-0.02}$ = 7.66

Slope of the graph (from B) = $\frac{2.41-1.49}{0.14-0.02}$ =7.66

Table 1: Readings for different output voltages for solution of different concentration of potassium dichromate

Molarity	Direct readings (Volts)		Final Readings (Volts)		Differential readings (Volts)	
	V.M*	D.M.M#	V.M	D.M.M	V.M	D.M.M
0.14	2.60	2.67	0.16	0.26	2.44	2.41
0.12	2.60	2.67	0.28	0.37	2.32	2.30
0.10	2.60	2.67	0.43	0.52	2.17	2.15
0.08	2.60	2.67	0.56	0.66	2.04	2.01
0.06	2.60	2.67	0.72	0.82	1.88	1.85
0.04	2.60	2.67	0.88	0.96	1.72	1.71
0.02	2.60	2.67	1.08	1.18	1.52	1.49
0.01	2.60	2.67	1.20	1.30	1.40	1.37

* V. M.: Digital Voltmeter in-built in the device

D.M.M.: Digital multimeter

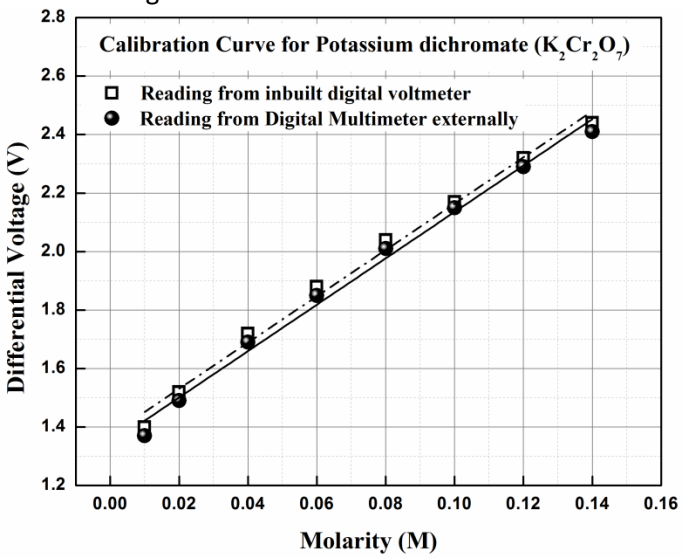

Fig. 2: Calibration curve between differential output voltage and Molarity for $K_2Cr_2O_7$

The slope of the graph represents the sensitivity of the colorimeter for potassium dichromate solution i.e., for unit change in molarity, change in output voltage is 7.66 V. From the origin software, the adj R^2 of the curve is found to be 0.99085 which is almost equal to 1. This suggests that the curve is linear. The limit of detection of the solution is found to be 0.01 M that is concentration less than the value of 0.01 M can't be detected by the colorimeter.

For Copper sulphate the readings that have been obtained are tabulated in Table 2. From the above tabulated values, we plot a graph shown in Fig. 3, taking Molarity (M) along -axis and output voltage (V) along Y-axis. Two Curves are drawn, one for the reading from the inbuilt voltmeter (A) and other from external digital multimeter (B). This curve can be divided into two portions- for concentration range 0.8 M - 1.0 M and 1.0 M - 1.6 M. For the first portion linearity is found to be 0.88462. For the second portion, the linearity is found to be 0.982.

The slope of the curve (A) = $\frac{(1.28-0.68)}{(1.5-1.2)} = 2$

The slope of the curve (B) = $\frac{(1.247-0.655)}{(1.5-1.2)} = 1.9$

These slopes represent the sensitivity of the colorimeter for copper sulphate solution that is for unit change in molarity, the change in output voltage is almost 2 volt. The limit of detection for the solution of Copper sulphate is found to be 1.0 M as for concentrations below that values the curve is not linear.

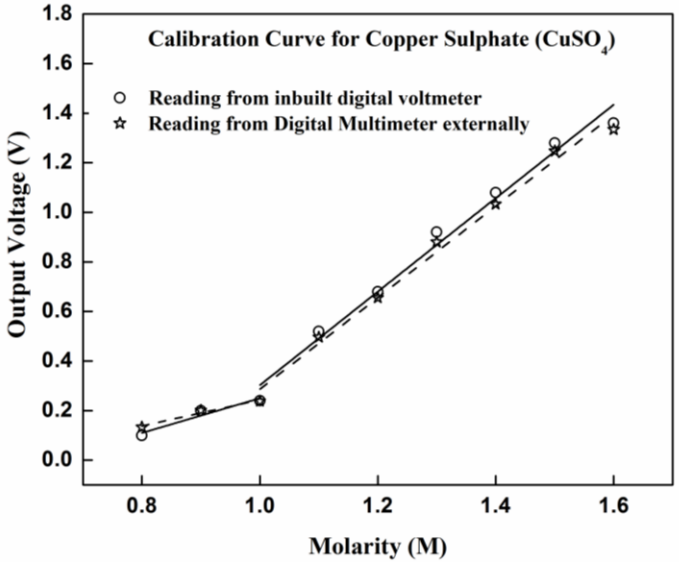

Fig. 3: Calibration curve between differential output voltage and Molarity for $CuSO_4$

In case of handling the two circuits, it has to be kept in mind that the power rating of each and every component of the circuit to minimize the damage due to high input voltage. Insulation from external light sources is an important aspect so that we can get more precise and accurate reading in our experiment. The experiment was, therefore, performed in a dark room to get error free results. Though we had placed a digital voltmeter to get the voltage across the output; we had also connected a digital multimeter externally for a better precision as the multimeter has lower least count than the voltmeter. However, there were some factors which could result in

some amount of error in the experiment. When the light enters the solution, it gets scattered and therefore some amount of light doesn't fall on the LDR which contribute to a little amount of error. Again, the apparatus that we used to make solutions of different concentrations might not be 100% accurate. Despite these inaccuracies the results are quite encouraging.

4. Conclusions

LED based chemical sensors and sensing devices have a broad range of applicability within the areas of health, security and environment. However, these have not yet been used and exploited to anything like their full capacity. LEDs are increasingly available in smaller packages, lower cost, high efficiency and availability at increasingly lower wavelengths. These continuing improvements will in turn facilitate the development of portable, autonomous, low-cost analytical devices and optical sensors that will open up various new applications. Clearly, LEDs will continue to be an increasingly important building block for future analytical devices and optical sensors. In the present work, the use of LEDs for constructing a digital colorimeter has been illustrated and the results obtained are quite encouraging.

5. Acknowledgement

The authors would like to acknowledge the Head and the faculty members of the Department of Physics for their timely help and discussion during the course of the project.

6. References

[1] https://en.wikipedia.org/wiki/Beer%E2%80%93Lambert_law

Bulletin of Physics Projects
Journal homepage: http://www.bbcphysics.in/index.php/journal

Synthesis of Sucrose ($C_{12}H_{22}O_{12}$), Sodium Chloride (NaCl) and Copper Sulphate ($CuSO_4$) single crystals by Solution Crystallization and X-Ray Diffraction study of Sucrose single crystals

Mrinmoy Goswami, Jyoti Barman , Shaheen Gulshanah and Dipsikha Kalita[#]

Department of Physics, B. Borooah College, Ulubari, Guwahati-781007, Assam, India

[#]E-mail address: dkalita93@gmail.com

Abstract

In this work an attempt has been made to grow single crystals of three different compounds viz., Sucrose ($C_{12}H_{22}O_{11}$), Copper sulphate ($CuSO_4$) and Sodium chloride (NaCl) by slow evaporation solution growth technique at room temperature and to identify their crystalline nature by using X-ray diffraction analysis. Here the lattice parameters of the grown crystals of Sucrose ($C_{12}H_{22}O_{11}$) have been determined by X-ray diffraction studies.

1. Introduction

The growth of crystal has been of great interest to physicists since long time because of their unique properties. The crystal growth yields a crystalline solid whose atoms and molecules are closely packed. Crystal growth involves a variety of research fields ranging from surface physics, crystallography and material sciences to condensed mater physics [1, 2].

Solution crystal growth is one of the important techniques to grow a variety of crystals when the material decomposes at the melting point and a suitable solvent is required to make a saturated solution at a desired temperature [3].

The solubility of a substance is the maximum amount of the solute that can be dissolved in a given quantity of solvent (water).Water can dissolve more solid substance at higher temperatures. This is because heated water molecules move farther apart, making room for more solid substance to dissolve. When no more of the solid substance can be dissolved, the solution is said to be supersaturated. As this solution cools, the water molecules move closer together again and there is less room for the solution to hold as much of the dissolved solid. Crystals begin to form and build on one another as the water lets go off the excess solute. This process is called recrystallization and depending upon conditions, one may obtain a mass of many small crystals or one large crystal.

During recrystallization, crystals start growing by a process called nucleation. Nucleation is the first step in growing a single crystal from a mother solution. This is achieved by taking the saturated solution to the supersaturated state. To get controlled growth, a seed crystal (small piece of single crystal from which a large crystal of the same material can be grown) is submerged in the solution. As the temperature of the solution continues to drop, more crystals will accumulate on the seed crystal.

The rate at which crystallization occurs, will affect crystal quality. The best crystals are the ones that grow slowly.
In the present work, Sucrose ($C_{12}H_{22}O_{11}$), Copper sulphate ($CuSO_4$) and Sodium chloride (NaCl) crystals have been grown by slow evaporation technique.

Sucrose is a naturally occurring carbohydrate found in plant parts. Other names of sucrose are sugar, saccharides etc. Sucrose has a white solid appearance and its molar mass is 342.30g. Its solubility in water is 2000g/L. Sucrose has a monoclinic crystal structure.

Sodium chloride is an ionic compound with the chemical formula NaCl, representing 1:1 ratio of sodium and chloride ions. Its molar mass is 58.44 gm/mole. Its solubility in water is 359 gm/litre. Its refractive index is 1.544 (at 589 nm). NaCl has a face centered cubic crystal structure. Copper Sulfate is an inorganic compound and its IUPAC name is Copper (II) Sulphate. Pentahydrate is the most commonly used salt having the chemical formula $CuSO_4.5H_2O$. The molar mass of cupric sulfate is 249.685 gm/mol. Its density is 2.286 gm/cm^3. Its solubility in water is 320 gm/litre (20°C). The lattice parameters of the grown crystal of Sucrose ($C_{12}H_{22}O_{11}$) have been determined by X-ray diffraction studies and the results obtained are reported here.

2. Experimental details:

For the crystallographic analysis we have prepared solution of $C_{12}H_{22}O_{11}$, $CuSO_4.5H2O$ and NaCl respectively. For NaCl solution, 40 grams (approx.) of salt is added in 100grams of water. For $CuSO_4$ solution, 110 grams (approx.) of salt is added in 100grams of water. Similarly for Sucrose solution, the ratio is 3:1 (Salt: Water). The following procedure is common for all the three salts that we have considered.

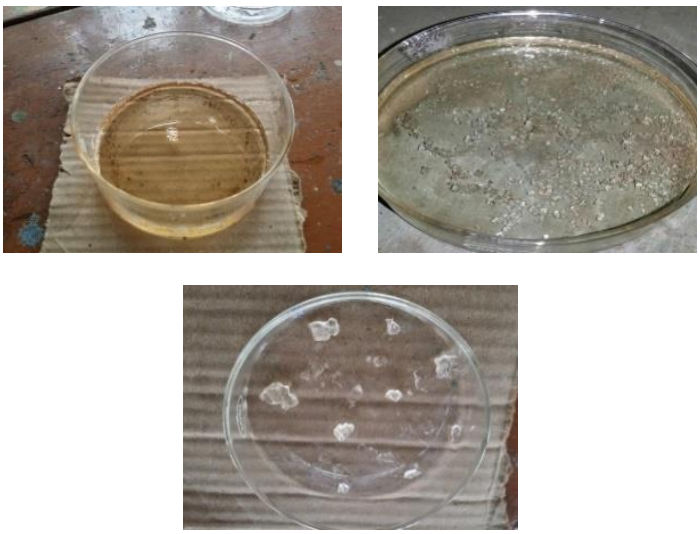

Fig1: Growth of Sucrose crystal

Fig. 2: Growth of Sodium chloride crystal

A certain amount of distilled water is taken in a beaker. The water is heated in an electric heater till the boiling point is achieved. Now our sample salt is added to the water in definite amount and it is allowed to dissolve completely. Again some additional amount is added in order to ensure if the solution has attained the supersaturated state. The solution is then filtered with the help of a filter paper. The filtrate is kept undisturbed for a couple of days for the crystal formation to occur. The same procedure is repeated for a number of times in order to obtain a bigger crystal. Fig.1-3 depicts the different stages of crystal growth.

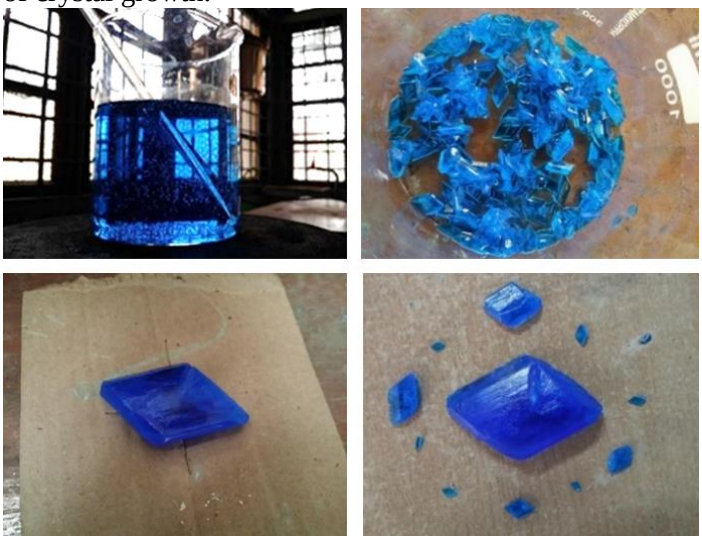

Fig. 3: Growth of Copper sulphate crystal

3. Results and Discussions:

The grown crystals of sucrose have been subjected to single crystal X-ray diffraction studies carried out by X-ray diffractometer. Fig.4 is the internal structure of the sucrose crystal obtained from X-ray diffractometer analysis.

From the analysis the lattice parameters were determined and compared with ideal values in Table1. The single crystal data indicates that the crystal belongs to monoclinic system. The values were compared with the ideal crystallographic data and are in good agreement with the reported values. The lattice parameters and the crystallographic angles could be determined using a

software WinGX. The results show that the sucrose crystal synthesized by solution crystallization method is a Monoclinic crystal and belongs to the space group $P2_1$.

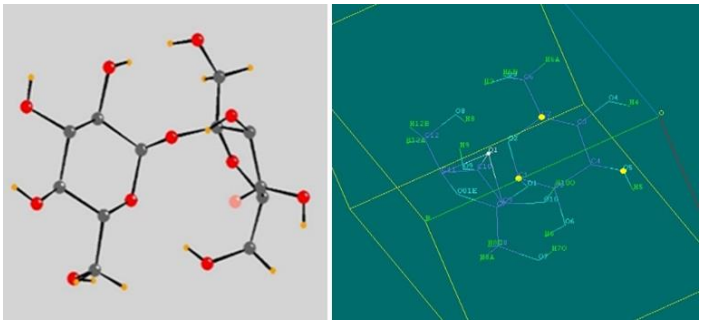

Fig. 4: Internal structure of the sucrose single crystal grown by solution crystallization

Table 1: Lattice parameters of sucrose single crystal

Lattice Parameters	From present work	Established values
a (Å)	7.87	7.76
b (Å)	8.79	8.7
c (Å)	10.96	10.86
α	90	90
β	102.5	102.93
ɤ	90.0	90.0
Crystal system	Monoclinic	Monoclinic
Space group	$P2_1$	$P2_1$

4. Conclusions:

The single crystal X-ray diffraction analysis of sucrose revealed that the crystal belongs to monoclinic system. The error obtained after the crystal analysis is 7% (approx.) which is within permissible limit. All the lattice parameters have also been found to match with the well-established experimental values.

5. Acknowledgement

The authors would like to thank the Head and all the faculties of the Department of Physics, B. Borooah College, Prof. Barindra Kr. Sarma, Retired Professor, Department of Physics, Gauhati University for their valuable suggestions and help during the work. The authors would also like to acknowledge the help received from Dr. Utpal Kr. Sarma, Department of Instrumentation and USIC, the Department of Chemistry, Gauhati University for rendering helps during the characterization of the sample.

6. References

[1] Z. Zhang,"Crystal growth". Proc. Natl. Acad. Sci. USA Vol. 96, pp. 11069–11070, September 1999

[2] Zhang, Z. Y., Niu, Q. & Shih, C. K. (1997) Phys. Rev. Lett. 80, 5381.

[3] Springer Handbook of crystal Growth, edited by edited by Govindhan Dhanaraj, Kullaiah Byrappa, Vishwanath Prasad, Michael Dudley

[4] https://www.chem.fsu.edu/chemlab/chm1046course/solubility.html